

# Study of the pion-mass dependence of $\rho$ -meson properties in lattice QCD

Kang Yu,<sup>1</sup> Yan Li,<sup>2</sup> Jia-Jun Wu,<sup>1,3</sup> Derek B. Leinweber,<sup>4</sup> and Anthony W. Thomas<sup>4</sup>

<sup>1</sup>*School of Physical Sciences, University of Chinese Academy of Sciences, Beijing 100049, China*

<sup>2</sup>*Department of Physics, University of Cyprus, 20537 Nicosia, Cyprus*

<sup>3</sup>*Southern Center for Nuclear-Science Theory (SCNT), Institute of Modern Physics, Chinese Academy of Sciences, Huizhou 516000, Guangdong Province, China*

<sup>4</sup>*Special Research Centre for the Subatomic Structure of Matter (CSSM), Department of Physics, University of Adelaide, Adelaide, South Australia 5005, Australia*

(Dated: November 8, 2023)

We collect spectra extracted in the  $I = \ell = 1$   $\pi\pi$  sector provided by various lattice QCD collaborations and study the  $m_\pi$  dependence of  $\rho$ -meson properties using Hamiltonian Effective Field Theory (HEFT). In this unified analysis, the coupling constant and cutoff mass, characterizing the  $\rho - \pi\pi$  vertex, are both found to be weakly dependent on  $m_\pi$ , while the mass of the bare  $\rho$ , associated with a simple quark-model state, shows a linear dependence on  $m_\pi^2$ . Both the lattice results and experimental data can be described well. Drawing on HEFT's ability to describe the pion mass dependence of resonances in a single formalism, we map the dependence of the phase shift as a function of  $m_\pi$ , and expose interesting discrepancies in contemporary lattice QCD results.

## I. INTRODUCTION

One of the most significant challenges in hadron physics is to understand the internal composition of diverse hadrons. However, because of the non-perturbative nature of the strong interaction in the low energy regime, the structure of hadrons within Quantum Chromodynamics (QCD) has remained unsolvable analytically. In order to develop insight into hadron structure and guide experimental work, a wide variety of phenomenological models have been developed. This includes the constituent quark model [1], the MIT [2] and cloudy bag models [3, 4] as well others based upon Schwinger-Dyson equations [5] and molecular [6] and hybrid [7] models. As it is often possible to adjust the parameters in these models in order to reproduce the limited experimental data, these models can typically not be distinguished solely on the basis of how well they describe experiments.

On the other hand, the approximate chiral symmetry of QCD means that the pion is a pseudo-Goldstone boson, with a much smaller mass,  $m_\pi$ , than other hadrons. Because the mass of the pion squared is proportional to the quark mass over a wide range, it is reasonable to expand certain physical variables in terms of  $m_\pi$ . For instance, the mass of a resonance  $R$  can be expressed perturbatively as follows:

$$m_R = \sum_{n=0}^{\infty} \alpha_n(\{g_i\}) m_\pi^{2n} + \Sigma_R(\{g_i\}, m_\pi), \quad (1)$$

where  $\{g_i\}$  is the set of free parameters of the model and  $\Sigma_R$  is the self-energy term. In the real world,  $m_\pi$  takes the fixed value  $\mu_\pi \approx 138.5$  MeV (for charged pions), and it is typically feasible to adjust the free parameters of a model,  $\{g_i\}$ , to reproduce the correct experimental value,  $m_R(\mu_\pi)$ . However, when we extend the model to unphysical pion masses these models may predict different values of  $m_R$  versus  $m_\pi$ . The dependence of various physical variables on  $m_\pi$  offers a fresh perspective in ex-

ploring the structure of hadrons in the non-perturbative regime [8]. As a result, it is of great significance to make measurements on  $m_R$  at unphysical  $m_\pi$  values.

Lattice QCD (LQCD) is a well-established non-perturbative formulation of QCD, defined on a finite and discretized volume of four-dimensional Euclidean space-time. Through simulation of the two-point Green functions of composite operators, one can obtain the finite volume spectrum of eigenvalues of the QCD Hamiltonian, with specific quantum numbers, as a function of  $m_\pi$ . We stress that such results are genuine predictions of QCD, even though the light quark masses do not take their physical values. Moreover, the phase shift in the infinite volume can then be obtained through the well-known Lüscher formula and its extensions [9–14].

LQCD has developed rapidly over the half century since Wilson's pioneering work was published in 1974 [15]. With the substantial progress in simulation algorithms and tremendous advances in computing power, many LQCD collaborations [16, 17] have extracted the finite volume spectra for various sets of quantum numbers, including the  $\rho$  meson, over a range of values of  $m_\pi$ .

Experimentally, the  $\rho$  meson is identified as a broad peak around  $\sqrt{s} = 770$  MeV in the invariant mass distribution of the isovector  $P$ -wave of  $\pi\pi$  scattering [18]. It is often identified as a confined  $q\bar{q}$  state, consistent with the constituent quark model. This picture is supported by several theoretical arguments, such as the large- $N_c$  limit of QCD [19–22]. Nevertheless, the sizable decay width,  $\Gamma_{\rho \rightarrow \pi\pi} \approx 140$  MeV [18], signifies the  $\rho$  meson's strong coupling to the  $\pi\pi$  channel. In other words, the observed peak structure results from the interaction between a  $q\bar{q}$  state, referred to as the bare  $\rho$ , and the  $\pi\pi$  continuum at the hadronic level. Consequently, a comprehensive study of the  $\rho$  meson necessitates an exploration of the  $\pi\pi$  scattering sector.

In the past decade, multiple LQCD groups have provided energy levels for the  $P$ -wave  $\pi\pi$  sector [23–36]. However, there has been little work collating spectra

from various collaborations [37, 38], particularly for  $N_f = 2 + 1$ , and performing a consistent unified analysis. That is the aim of this paper.

The Lüscher formula is the most practical way to relate lattice calculations to the elastic scattering phase shifts of two spinless particles. Therefore, when dealing with a system containing only one  $\pi\pi$  channel, it is sufficient to utilize the standard Lüscher formula to relate the finite volume spectrum to the phase shifts. However, in our present study, we also aim to incorporate the  $\omega\pi$  channel, in order to assess its impact. While it is not an open channel, it does generate the leading non-analytic behaviour of the  $\rho$  mass as a function of  $m_\pi$ . For the multi-channel case, other approaches that are equivalent to the Lüscher formalism up to exponentially suppressed corrections might offer greater convenience. As an example, we mention that the unitarized chiral perturbation theory can calculate the finite volume spectrum through the pole position of the T matrix defined in the finite volume as shown in Refs. [39, 40].

Alternatively, Hamiltonian effective field theory (HEFT) incorporates the Lüscher formalism and establishes a connection between the scattering process in infinite volume and the finite volume spectrum of the system [41]. For multi-channel scattering, the advantages and practicality of HEFT have been demonstrated in studies of various resonances, including the Roper [42, 43], the  $\Lambda(1405)$  [44], the  $N^*(1535)$  [45] and the  $D_s^*(2317/2460)$  [46]. Because the Hamiltonian operates within the Fock space, effectively describing interactions among various different channels, the HEFT approach has two unique advantages. 1) It provides insight into the composition of the eigenstates through the strength of various components of the eigenvectors. 2) It also enables an examination of the quark-mass dependence of resonance properties in a single formalism, enabling this unified analysis.

Here, we consistently analyze the spectra provided by several different LQCD collaborations using the HEFT framework, drawing on results extracted in the rest frame [47], moving frame and elongated frames [48]. Motivated by the physical picture mentioned, the Hamiltonian employed here is studied within a framework that involves a bare  $\rho$ , as well as  $\pi\pi$  and  $\omega\pi$  channels. We obtain the bare  $\rho$  mass in various regularization schemes from the lattice energy levels and investigate its dependence on  $m_\pi$ . We observe that the linear slope of the bare  $\rho$  mass with respect to  $m_\pi^2$  is minimally affected by scheme dependence. Furthermore, we investigate the composition of the  $\rho$  meson, using the eigenvector of the eigen-energy state closest to the physical  $\rho$  mass. Finally, we illustrate interesting discrepancies in contemporary lattice QCD calculations.

The paper is organized as follows. In Sec. II we provide an overview of the HEFT formulation and proceed to construct the finite volume Hamiltonian for the specific case under investigation. Section III presents the results of the numerical analysis and examines the dependence

of various variables on  $m_\pi$ . Finally, in Sec. IV, we draw the discussion to a close with a concise summary and a suggestions for further analysis.

## II. FORMALISM

### A. Hamiltonian model

The Hamiltonian in the center of mass frame of the interacting system is divided into two parts as follows,

$$H = H_0 + H_I, \quad (2)$$

where  $H_0$  is the non-interacting part, and  $H_I$  is the interaction part. In this work, we include a bare  $\rho$  meson, which can be identified as a  $q\bar{q}$  state, as well as two coupled channels,  $\pi\pi$  and  $\pi\omega$ . In the infinite volume, characterized by  $SO(3)$  symmetry, it is most convenient to express the interaction in the  $JLS$  basis defined as [49]

$$|\alpha; k^*, JM\ell S\rangle = A_\alpha \sum_{m\sigma\sigma_1\sigma_2} C_{\ell S}(JM; m\sigma) C_{s_1 s_2}(S\sigma; \sigma_1\sigma_2) \times \int d\hat{\mathbf{k}}^* Y_{\ell m}(\hat{\mathbf{k}}^*) |\alpha; \mathbf{k}^*, \sigma_1\sigma_2\rangle, \quad (3)$$

where  $C_{j_1 j_2}(jm; m_1 m_2)$  is the Clebsch-Gordon (CG) coefficient of the  $SU(2)$  group,  $Y_{\ell m}$  are the normalized spherical harmonics functions and  $|\alpha; \mathbf{k}^*, \sigma_1\sigma_2\rangle$  indicates the  $\alpha = \pi\pi$  or  $\pi\omega$  channels, with relative momentum  $\mathbf{k}^*$  and  $z$ -components of the spins of two particles,  $\sigma_1$  and  $\sigma_2$ , respectively. (For convenience, the quantities with an asterisk in this paper are all defined in the center of mass frame.) In addition,  $A_\alpha$  is the normalization factor that equals  $\frac{1}{\sqrt{2}}$  if  $\alpha = \pi\pi$  and otherwise is unity,  $m$  and  $\sigma$  are the  $z$ -components of the orbital angular momentum and total spin, respectively,  $S_1$  and  $S_2$  are the spins of the particles in channel  $\alpha$  and  $J$ ,  $M$ ,  $\ell$  and  $S$  are the total angular momentum, the  $z$ -component of the total angular momentum, orbital angular momentum, and total spin, respectively. The  $|\alpha; k^*, M\rangle$  is normalized as,

$$\langle \alpha; k^*, JM\ell S | \alpha'; k^{*'}, JM'\ell S \rangle = \frac{\delta(k^* - k^{*'})}{k^{*2}} \delta_{\alpha\alpha'} \delta_{MM'}. \quad (4)$$

In general, there are interactions between the bare state and the two-particle channels as well as within and between the coupled channels. However, in this study, most of the energy levels and phase shifts are in the resonance region, so the dominant interaction is that between the bare state and two-particle channels. In addition, given the limited data concerning the energy levels from LQCD as well as experimental observables, we find that, in practice, the existing data can be described well without introducing channel-channel interactions. For this reason, the  $\pi\pi - \pi\pi$ ,  $\pi\pi - \pi\omega$  and  $\pi\omega - \pi\omega$   $t/u$ -channel interactions are neglected.

Because of the definite  $J^P$  quantum number of the bare  $\rho$  meson, it is sufficient to focus on the Hamiltonian in the subspace spanned by  $|\alpha = \pi\pi; k^*, J = 1, M, \ell = 1, S = 0\rangle$  and  $|\alpha = \omega\pi; k^*, J = 1, M, \ell = 1, S = 1\rangle$ . For convenience, the  $JLS$  indices will be suppressed hereafter.

The free energy part of the Hamiltonian in this subspace,  $H_0$ , is given by,

$$H_0 = \sum_M m_\rho^B |\rho_B, M\rangle \langle \rho_B, M| + \sum_{\alpha, M} \int k^{*2} dk^* (E_{\alpha_1}(k^*) + E_{\alpha_2}(k^*)) |\alpha; k^*, M\rangle \langle \alpha; k^*, M|, \quad (5)$$

where  $|\rho_B, M\rangle$  indicates the bare  $\rho$  state with  $z$ -component of spin,  $M$ ,  $E_{\alpha_i}(k) = \sqrt{k^2 + m_{\alpha_i}^2}$  with  $\alpha_i = \pi$  or  $\omega$ ,  $m_{\alpha_i}$  is for the mass of the particle in the  $\alpha$  channel and  $m_\rho^B$  is the mass of the bare single-particle basis state.

The interacting part,  $H_I$ , is given by,

$$H_I = \sum_{\alpha, M} \int k^{*2} dk^* \{ V_\alpha(k^*) |\rho_B, M\rangle \langle \alpha; k^*, M| + \text{h.c.} \}, \quad (6)$$

where the interaction term  $V_\alpha$  is independent of  $M$ , as a consequence of the Wigner-Eckart theorem, and given by

$$V_{\pi\pi}(k^*) = \frac{g_{\rho\pi\pi}}{2\pi\sqrt{3}} \frac{k^*}{\sqrt{m_\rho^B E_\pi(k^*)}} u_{\pi\pi}(k^*), \quad (7)$$

$$V_{\omega\pi}(k^*) = \frac{g_{\omega\rho\pi}}{2\pi\sqrt{6}} \frac{k^* \sqrt{m_\rho^B}}{\sqrt{E_\pi(k^*) E_\omega(k^*)}} u_{\omega\pi}(k^*), \quad (8)$$

where  $u_{\pi\pi}$  and  $u_{\omega\pi}$  are the form factors parameterizing the internal structure of hadrons and ensuring the convergence of loop integrals. Here, the usual dipole form factors are used [50, 51],

$$u_{\pi\pi}(k) = \left( \frac{\Lambda_{\rho\pi\pi}^2}{k^2 + \Lambda_{\rho\pi\pi}^2} \right)^2, \quad (9)$$

$$u_{\omega\pi}(k) = \left( \frac{\Lambda_{\omega\rho\pi}^2 - \mu_\pi^2}{k^2 + \Lambda_{\omega\rho\pi}^2} \right)^2, \quad (10)$$

where  $\mu_\pi = 138.5\text{MeV}$  is the physical mass of the pion.

The scattering T-matrix, defined by  $S_{fi} = \delta_{fi} - 2\pi i \delta^4(p_f - p_i) T_{fi}$ , can be obtained from the partial wave Lippmann-Schwinger equation [41, 50, 52],

$$T_{\alpha\beta}(p, q, E) = V_{\alpha\beta}(p, q, E) + \sum_\gamma \int k^2 dk \frac{V_{\alpha\gamma}(p, k, E) T_{\gamma\beta}(k, q, E)}{E - E_{\gamma_1}(k) - E_{\gamma_2}(k) + i\varepsilon}, \quad (11)$$

where  $V_{\alpha\beta}$  comes from bare  $\rho$  exchange in the  $s$ -channel and is given by

$$V_{\alpha\beta}(p, q, E) = \frac{V_\alpha^*(p) V_\beta(q)}{E - m_\rho^B}. \quad (12)$$

with  $V_\alpha$  defined in Eqs.(7) and (8). In the present case  $T_{\pi\pi, \pi\pi}(p, q; E)$  can be obtained analytically

$$T_{\pi\pi, \pi\pi}(p, q; E) = V_{\pi\pi}^*(p) G(E) V_{\pi\pi}(q), \quad (13)$$

where  $G(E)$  is the full propagator of the  $\rho$  meson defined by,

$$G(E)^{-1} = E - m_\rho^B - \Sigma(E), \quad (14)$$

with the self-energy

$$\Sigma(E) = \Sigma_{\pi\pi}(E) + \Sigma_{\omega\pi}(E), \quad (15)$$

$$\Sigma_{\pi\pi}(E) = \int q^2 dq \frac{|V_{\pi\pi}(q)|^2}{E - 2E_\pi(q) + i\varepsilon}, \quad (16)$$

$$\Sigma_{\omega\pi}(E) = \int q^2 dq \frac{|V_{\omega\pi}(q)|^2}{E - E_\pi(q) - E_\omega(q) + i\varepsilon}. \quad (17)$$

The partial-wave phase shift,  $\delta(E)$ , for the  $P$ -wave  $\pi\pi \rightarrow \pi\pi$  elastic scattering is then given by,

$$e^{2i\delta(E)} = 1 - i \frac{\pi \bar{p} E}{2} \bar{p} T_{\pi\pi, \pi\pi}(\bar{p}, \bar{p}; E), \quad (18)$$

$$\delta(E) = \arctan \left[ \frac{\text{Im} \Sigma_{\pi\pi}(E)}{E - m_\rho^B - \text{Re} \Sigma(E)} \right] \pmod{\pi}, \quad (19)$$

where  $\bar{p} = \sqrt{E^2/4 - m_\pi^2}$  is the on-shell momentum. The pole position of the  $\rho$ -resonance is located in the lower half plane of the unphysical Riemann sheet of the  $\pi\pi$ -channel but the first Riemann sheet of the  $\omega\pi$ -channel and determined by solving the equation

$$0 = E - m_\rho^B - \Sigma(E). \quad (20)$$

## B. The Hamiltonian in finite volume

To obtain the energy levels in finite volume, we need to construct the finite volume Hamiltonian (FVH). Two major problems are encountered. Firstly, the correspondence between the Fock spaces spanned by the states with continuous and discrete momentum and secondly, the symmetry is reduced from the  $O(3)$  group to a finite subgroup,  $G$ , for the finite volume. As a result,  $J$  and  $M$  are no longer good quantum numbers. In Refs.[47, 48], the standard formalism for the rest, moving and elongated frames were presented. Here we give a brief introduction to those aspects relevant to the present work.

To obtain the FVH in terms of the states with discrete momentum, one needs to make the following substitutions in Eqs.(5) and (6). First one sets

$$|\rho_B, M\rangle \rightarrow |\rho_B, M\rangle_L, \quad (21)$$

because the bare  $\rho$  single-particle state does not change. However, it is very different for the two-particle state,

$$|\alpha; k^*, M\rangle \rightarrow \sqrt{\frac{V}{(2\pi)^3}} |\alpha; e_{\mathbf{n}}, M\rangle, \quad (22)$$

and

$$\int d^3\mathbf{k}^* \rightarrow \frac{(2\pi)^3}{V} \sum_{\mathbf{n} \in \mathbb{Z}^3}, \quad (23)$$

where  $V = \eta L^3$  is the volume of the box, with elongation factor  $\eta$ , and  $e_{\mathbf{n}}$  denotes a degenerate shell of the non-interacting Hamiltonian in the rest frame, because those states with the same  $e_{\mathbf{n}}$  share the same  $|\mathbf{k}^*(\mathbf{n})|$ . For example, in the rest frame of a cubic box,  $\mathbf{k}^* = \frac{2\pi}{L}\mathbf{n}$  and hence  $e_{\mathbf{n}} = \mathbf{n}^2$ . However, for the general case,  $\mathbf{k}^*(\mathbf{n})$  and hence  $e_{\mathbf{n}}$  are not that simple. A detailed discussion of  $e_{\mathbf{n}}$  and  $\mathbf{k}^*(\mathbf{n})$  can be found in Ref. [48] and a summary is given in Appendix A. The finite volume basis vector,  $|\alpha; e_{\mathbf{n}}, M\rangle$ , is given by an expression analogous to Eq. (3)

$$|\alpha; e_{\mathbf{n}}, M\rangle = A_{\alpha} \sum_{m\sigma_1\sigma_2} C_{\ell S}(JM; m\sigma) C_{s_1 s_2}(S\sigma; \sigma_1\sigma_2) \times \sum_{\mathbf{n} \in \{\hat{e}_{\mathbf{n}}\}} Y_{\ell m}(\hat{\mathbf{k}}^*(\mathbf{n})) |\mathbf{k}^*(\mathbf{n}), \sigma_1\sigma_2\rangle, \quad (24)$$

with  $J = 1$ ,  $\ell = 1$  and  $S = 0/1$  for  $\alpha = \pi\pi/\omega\pi$ , respectively. Here  $\{\hat{e}_{\mathbf{n}}\}$  denotes the set of integer vectors with the same  $e_{\mathbf{n}}$ .

Note that the states defined in Eq. (3) with different values of  $JM\ell S$  are orthogonal, which is not the case in the finite volume since  $O(3)$  symmetry is broken. Thus, it is necessary to construct an orthogonal basis  $|\alpha; e_{\mathbf{n}}, \Gamma, a\rangle$  furnishing an irreducible representation  $\Gamma$  of  $G$ . Such states take linear combinations of the basis states  $|\alpha; e_{\mathbf{n}}, M\rangle$  with reduction coefficients  $C_{\Gamma, G}$  [48, 53],

$$|\alpha; e_{\mathbf{n}}, \Gamma, a\rangle := \sqrt{\frac{1}{Z_{\Gamma}(e_{\mathbf{n}})}} [C_{\Gamma, G}]_{M, a} |\alpha; e_{\mathbf{n}}, M\rangle, \quad (25)$$

$$\langle \alpha; e_{\mathbf{n}}, \Gamma, a | \alpha'; e'_{\mathbf{n}}, \Gamma', a' \rangle = \delta_{\alpha\alpha'} \delta_{e_{\mathbf{n}}e'_{\mathbf{n}}} \delta_{\Gamma\Gamma'} \delta_{aa'}, \quad (26)$$

where  $Z_{\Gamma}(e_{\mathbf{n}})$  is the normalization factor. In general there should be another index denoting the multiplicity of  $\Gamma$ , but in the present case that additional index is always 1 and hence it will be suppressed. The reduction coefficients relevant to the work reported here are shown in Appendix C. Similarly,

$$|\rho_B, \Gamma, a\rangle = [C_{\Gamma, G}]_{M, a} |\rho_B, M\rangle_L, \quad (27)$$

satisfying

$$\langle \rho_B, \Gamma, a | \rho_B, \Gamma', a' \rangle = \delta_{\Gamma\Gamma'} \delta_{aa'}. \quad (28)$$

With these well-defined orthogonal basis states  $|\rho_B, \Gamma, a\rangle$  and  $|\alpha; e_{\mathbf{n}}, \Gamma, a\rangle$ , the FVH in the rest frame for a given irreducible representation,  $\Gamma$ , (note that because of the Wigner-Eckart theorem, the eigenvalue is independent of the “ $a$ ” index, which is therefore suppressed) is

given by

$$H^{\text{fin}} = \sum_{\Gamma} (H_{0, \Gamma}^{\text{fin}} + H_{I, \Gamma}^{\text{fin}}), \quad (29)$$

$$H_{0, \Gamma}^{\text{fin}} = m_{\rho}^B |\rho_B, \Gamma\rangle \langle \rho_B, \Gamma| + \sum_{\alpha; e_{\mathbf{n}}} |\alpha; e_{\mathbf{n}}, \Gamma\rangle \langle \alpha; e_{\mathbf{n}}, \Gamma| \times (E_{\alpha_1}(|\mathbf{k}^*(\mathbf{n})|) + E_{\alpha_2}(|\mathbf{k}^*(\mathbf{n})|)), \quad (30)$$

$$H_{I, \Gamma}^{\text{fin}} = \sum_{\alpha, e_{\mathbf{n}}} V_{\alpha, \Gamma}^{\text{fin}}(|\mathbf{k}^*(\mathbf{n})|) |\rho_B, \Gamma\rangle \langle \alpha; e_{\mathbf{n}}, \Gamma| + \text{h.c.} \quad (31)$$

Alternatively, these equations may be expressed in matrix form

$$H_{0\Gamma}^{\text{fin}} + H_{I\Gamma}^{\text{fin}} = \begin{pmatrix} m_{\rho}^B & v^T \\ v & h_0 \end{pmatrix} \quad (32)$$

$$v^T = (V_{\pi\pi, \Gamma}^{\text{fin}}(|\mathbf{k}^*(\mathbf{n}_1)|), V_{\pi\pi, \Gamma}^{\text{fin}}(|\mathbf{k}^*(\mathbf{n}_2)|), \dots, \dots, V_{\omega\pi, \Gamma}^{\text{fin}}(|\mathbf{k}^*(\mathbf{n}'_1)|), V_{\omega\pi, \Gamma}^{\text{fin}}(|\mathbf{k}^*(\mathbf{n}'_2)|), \dots) \quad (33)$$

$$h_0 = \text{diag}(2E_{\pi}(|\mathbf{k}^*(\mathbf{n}_1)|), 2E_{\pi}(|\mathbf{k}^*(\mathbf{n}_2)|), \dots, E_{\pi}(|\mathbf{k}^*(\mathbf{n}'_1)|) + E_{\omega}(|\mathbf{k}^*(\mathbf{n}'_1)|), E_{\pi}(|\mathbf{k}^*(\mathbf{n}'_2)|) + E_{\omega}(|\mathbf{k}^*(\mathbf{n}'_2)|), \dots). \quad (34)$$

In principle the FVH is countably infinite-dimensional, while in practice it is found that the contribution of high-energy states to the low-lying eigenvalues of interest is negligible. Therefore, the matrix can be truncated by excluding the states with momentum higher than a certain value  $k_{\text{cut}}^*$  to obtain a finite-dimensional matrix.

By comparing Eqs.(3),(6),(24),(25) and (31),  $V_{\alpha, \Gamma}^{\text{fin}}(|\mathbf{k}^*(\mathbf{n})|)$  is written as,

$$V_{\alpha, \Gamma}^{\text{fin}}(e_{\mathbf{n}}) = \sqrt{\frac{(2\pi)^3}{V}} J_{\alpha}(e_{\mathbf{n}}) \sqrt{Z_{\Gamma}(e_{\mathbf{n}})} V_{\alpha}(|\mathbf{k}^*(\mathbf{n})|), \quad (35)$$

where the Jacobian,  $J_{\alpha}$ , just appears for a moving system, with the expression shown in Eq. (A2).

### C. Fitting Formulas

In the present work, we fit the eigenvalues of the FVH,  $E^{\text{H}}$ , to the lattice spectrum,  $E_{\text{cm}}^{\text{lat}}$ , with the usual least- $\chi^2$  strategy. That is, we minimize the  $\chi^2$  defined as

$$\chi^2 = (E^{\text{H}} - E_{\text{cm}}^{\text{lat}})^T \mathbb{C}^{-1} (E^{\text{H}} - E_{\text{cm}}^{\text{lat}}), \quad (36)$$

where  $\mathbb{C}$  denotes the covariance matrix of the lattice spectrum. It should be noted that  $E_{\text{cm}}^{\text{lat}}$  is the spectrum that has been transformed into the rest frame. If a certain energy level,  $E_n^{\text{lat}}$ , is extracted from the composite operator with  $\mathbf{P} \neq 0$ , it needs to be converted to  $E_{\text{cm}, n}^{\text{lat}}$  through

$$E_{\text{cm}, n}^{\text{lat}} = \sqrt{(E_n^{\text{lat}})^2 - \mathbf{P}^2}. \quad (37)$$

In our model, there are five parameters, including the bare mass,  $m_{\rho}^B$ , two coupling constants  $g_{\rho\pi\pi}$  and  $g_{\omega\rho\pi}$ , defined in Eqs. (7) and (8), and two cut-off parameters  $\Lambda_{\rho\pi\pi}$  and  $\Lambda_{\omega\rho\pi}$ , defined in Eqs. (9) and (10), respectively.

### D. Formulas for the $m_\pi$ dependence

To extrapolate the results of the lattice calculations to the physical region, one needs to investigate the  $m_\pi$ -dependence of the properties of the  $\rho$  meson. This issue has been previously discussed in some studies [51, 54–56] and in this paper it will be studied within the framework of HEFT. As discussed in Ref. [55], in the framework of Chiral Perturbation Theory, the mass of the  $\rho$  is a function of  $m_\pi$  of the form

$$m_\rho^p = c'_0 + c'_1 m_\pi^2 + c'_2 m_\pi^3 + c'_3 m_\pi^4 \ln\left(\frac{m_\pi^2}{m_\rho^2}\right) + \mathcal{O}(m_\pi^4), \quad (38)$$

where  $m_\rho^p$  is related to the pole mass of the  $\rho$ , corresponding to the real part of the pole of the T-matrix in the complex plane. In general,  $m_\rho^p$  is different from the usual Breit-Winger mass,  $m_\rho^{\text{BW}}$ , which is defined as the real energy at which the phase shift is 90 degrees. For the present case, however, the difference is negligible.

As discussed in Refs. [51, 55], the quark mass operator only contributes to the  $m_\pi^2$  term in Eq. (38) up to  $\mathcal{O}(m_\pi^4)$ , with the other two terms arising from pion-loop self-energies. The  $m_\pi^3$  term comes from the  $\omega\pi$  loop, involving a vector-vector-pseudoscalar ( $VVP$ ) vertex, while both  $\pi\pi$  and  $\omega\pi$  loops contribute to the log term. Within the present framework, the pole of the T-matrix is determined by Eq. (20), which tells us that

$$m_\rho^p \approx m_\rho^{\text{B}} + \text{Re}(\Sigma(m_\rho^p)). \quad (39)$$

Here “ $\approx$ ” indicates that we just use the real part of the pole,  $m_\rho^p$ , for calculating the self-energy. For the later calculations in Sec.(III), we will first get  $m_\rho^p$  by solving Eq.(20) and then estimate the real part of the self-energy at the pole position by  $m_\rho^p - m_\rho^{\text{B}}$ . Comparing Eq. (38) and Eq. (39), the bare mass  $m_\rho^{\text{B}}$  is a quadratic function of  $m_\pi$  at the leading order,

$$m_\rho^{\text{B}}(m_\pi) = c_0 + c_1 m_\pi^2. \quad (40)$$

In our analysis, this equation will be used to study the extracted  $m_\rho^{\text{B}}$  as function of  $m_\pi$ .

It is important to note that Eq. (40) is derived from the continuum field theory. In principle, to extrapolate the results obtained from lattice, the residual lattice artifacts should be estimated and removed. For  $\mathcal{O}(a)$ -improved actions, the effect of the finite lattice spacing can be estimated as follows,

$$m_\rho^{\text{B}}(m_\pi; a) = c_0 + c_1 m_\pi^2 + \xi a^2, \quad (41)$$

where  $\xi$  characterizes the rate at which it approaches the continuum limit and may vary from collaboration to collaboration as different fermion actions are used.

## III. NUMERICAL RESULTS AND DISCUSSION

### A. The LQCD Data

The finite volume spectra for the  $I = \ell = 1$   $\pi\pi$  sector with dynamical fermions at various pion masses have been provided by several LQCD collaborations over the past decade, including PACS-CS (2011,  $N_f = 2+1$ ) [24], HSC (2013,  $N_f = 2+1$ ) [27], HSC (2015,  $N_f = 2+1$ ) [26], Guo *et al.* (2016,  $N_f = 2$ ) [32], MILC(2016,  $N_f = 2+1$ ) [33], C. Alexandrou *et al.* (2017,  $N_f = 2+1$ ) [29], J. Bulava *et al.* (2019,  $N_f = 2+1$ ) [34], and ETMC (2020,  $N_f = 2+1(+1)$ ) [28]. Further details and energy levels are shown in Table I and the panels in Fig. 1, as well as all figures in Appendix D, where HEFT is fit to the various lattice data sets.

### B. Three Fitting Schemes

In this work, our aim is to study the properties of the  $\rho$  meson by investigating the pion mass dependence of various relevant variables. In the HEFT framework, we have five free parameters which may be used to fit the lattice data with different pion masses. However, for each specific pion mass, there are only a few energy levels. In addition, the  $\omega\pi$  contribution is considerably weaker than that of the  $\pi\pi$  channel, since the threshold of  $\omega\pi$  is higher than the  $\rho$  mass. Consequently, we first adopt scheme A, wherein the interaction  $V_{\omega\pi}$  is turned off, i.e.,  $g_{\omega\rho\pi} \equiv 0$ , while  $m_\rho^{\text{B}}$ ,  $g_{\rho\pi\pi}$ , and  $\Lambda_{\rho\pi\pi}$  are treated as free fitting parameters. The finite volume spectra provided by various collaborations involving different  $\pi$  masses are each fit independently. Using scheme A, it is found that both  $g_{\rho\pi\pi}$  and  $\Lambda_{\omega\rho\pi}$  show a very weak dependence on  $m_\pi$ , while  $m_\rho^{\text{B}}$  is strongly dependent on  $m_\pi$ , as anticipated earlier.

Building upon the results found using scheme A, in scheme B both  $g_{\rho\pi\pi}$  and  $\Lambda_{\rho\pi\pi}$  are fixed to be independent of  $m_\pi$ , in accord with standard practice in chiral effective field theory.  $m_\rho^{\text{B}}$  is allowed to vary. As a result, this approach effectively combines spectra from various pion masses provided by different LQCD groups together in a unified analysis to constrain the variation of the bare mass,  $m_\rho^{\text{B}}$ , with  $m_\pi$ .

Finally, the contribution of the  $\omega\pi$  channel is examined in scheme C. In this case  $V_{\omega\pi}$  is switched on, however, the two coupling constants,  $g_{\rho\pi\pi}$  and  $g_{\omega\rho\pi}$ , as well as two cutoffs,  $\Lambda_{\rho\pi\pi}$  and  $\Lambda_{\omega\rho\pi}$ , are taken to be independent of  $m_\pi$ , while only  $m_\rho^{\text{B}}$  is permitted to vary in the fitting. These three schemes are summarized in Table II.

TABLE I. Details of the spectra by different collaborations. Columns, from left to right, show collaboration and year of spectra, pion mass ( $m_\pi$ ), number of flavor ( $N_f$ ), lattice size ( $L$ ) and spacing ( $a$ ) in fm, employed gauge and fermion actions, number of energy levels ( $N_{\text{lvl}}$ ), and energy level extraction method. Besides, the spectra provided by Guo *et al.* are extracted in a elongated box with factor  $\eta = 1, \frac{7}{6}, \frac{4}{3}$  for  $m_\pi = 226$  MeV, and  $\eta = 1, 1.25, 2$  for  $m_\pi = 315$  MeV.

COLLAB.(Year)	$m_\pi$ (MeV)	$N_f$	$L$ (fm)	$a$ (fm)	Action	$N_{\text{lvl}}$	method
J.Bulava(2018)	200	2+1	4.1	0.06	improved Lüscher-Weisz gauge improved Wilson fermion	17	GEVP
	220		4.1	0.09		21	
	280		3.1	0.06		15	
HSC(2013)	391	2+1	1.9	0.12	Symanzik-improved gauge anisotropic Clover fermion	7	GEVP
			2.4	0.12		10	
			2.9	0.12		14	
HSC(2015)	236		3.8	0.12		23	
HSC(2023)	330		2.8	0.12		17	
MILC(2016)	176	2+1	5.4	0.09	improved Lüscher-Weisz gauge staggered fermion	9	GEVP
	247		3.4	0.09		9	
	248		3.4	0.09		9	
	301		2.7	0.09		9	
	346		2.4	0.09		7	
	276		3.7	0.12		9	
ETMC(2020)	322	2+1+1	2.8	0.09	Iwasaki gauge twisted-mass Wilson fermion	18	GEVP
	386		2.1	0.09		16	
	262		2.6	0.08		13	
	302		3.9	0.08		23	
	376		2.6	0.08		14	
C.Alexandru(2017)	316	2+1	3.6	0.11	Symanzik-improved gauge clover Wilson fermion	15	GEVP
PACS-CS(2011)	411	2+1	2.9	0.09	Iwasaki gauge improved Wilson fermion	6	Exp Fit
Guo(2016)	226	2	2.9	0.12	Lüscher-Weisz gauge nHYP-smearred Clover fermion	8	GEVP
	315					20	

TABLE II. Outline of the fitting schemes.

	$m_\rho^{\text{B}}$	$g_{\rho\pi\pi}, \Lambda_{\rho\pi\pi}$	$g_{\omega\rho\pi}, \Lambda_{\omega\rho\pi}$
A	free	free	off
B	free	fixed	off
C	free	fixed	fixed

## C. Fitting Results

### 1. Results for Scheme A

Recall that in scheme A, the  $\rho - \omega\pi$  interaction is turned off and the lattice spectra are fit using three free parameters  $m_\rho^{\text{B}}$ ,  $g_{\rho\pi\pi}$ , and  $\Lambda_{\rho\pi\pi}$ . The fitted spectra as a function of spatial extent,  $L$ , are shown by the blue curves in Fig. 1 for  $m_\pi = 200$  MeV as an illustration. All other fits are presented in Appendix D. The corresponding fitted parameter values are outlined in the columns dedicated to scheme A in Table III. In addition, the pion mass dependence of the three parameters,  $g_{\rho\pi\pi}$ ,  $\Lambda_{\rho\pi\pi}$ , and  $m_\rho^{\text{B}}$  are shown in Fig. 2 and in the top panel of Fig. 3, respectively.

From Fig. 2, it is found that the cut-off parameter  $\Lambda_{\rho\pi\pi}$  and the dimensionless coupling constant,  $g_{\rho\pi\pi}$ , both show

a weak dependence on  $m_\pi$ . In contrast, it is worth noting that for each  $m_\pi$ ,  $\Lambda_{\rho\pi\pi}$  exhibits a large uncertainty. Indeed, in some cases the upper uncertainty does not display in MINUIT2, which means that even for very large values of the cut-off, we can still find a reasonable fit for the energy levels. This observation suggests that the eigenvalue of the FVH around the region of the  $\rho$  mass is insensitive to  $\Lambda_{\rho\pi\pi}$ . This is consistent with the findings reported in Ref. [58], where the  $\Lambda$ -dependence of the eigenvalue and eigenvector are investigated in detail. A more common [27] dressed coupling constant,  $g_{\rho\pi\pi}^{\text{BW}}$ , is defined by

$$g_{\rho\pi\pi}^{\text{BW}} \equiv \sqrt{\frac{6\pi(m_\rho^{\text{BW}})^2}{\bar{p}}} \Gamma_{\rho \rightarrow \pi\pi}^{\text{BW}}, \quad (42)$$

where  $\bar{p}$  is defined by  $2\sqrt{\bar{p}^2 + m_\pi^2} = m_\rho^{\text{BW}}$  and  $\Gamma_{\rho \rightarrow \pi\pi}^{\text{BW}}$  is the partial width of the resonance in the Breit Wigner parameterizations. In our model,  $g_{\rho\pi\pi}^{\text{BW}}$  depends on both the value of  $g_{\rho\pi\pi}$  and the form factor  $u_{\pi\pi}$ , which is determined by  $\Lambda_{\rho\pi\pi}$ . As a result, the slight  $m_\pi$ -dependence seen in  $g_{\rho\pi\pi}$  and  $\Lambda_{\rho\pi\pi}$  clearly implies that the value of  $g_{\rho\pi\pi}^{\text{BW}}$ , approximated to be around 6.0, remains independent of  $m_\pi$ . This conclusion is consistent with the discussions presented in prior works, such as Refs. [29, 31, 33].

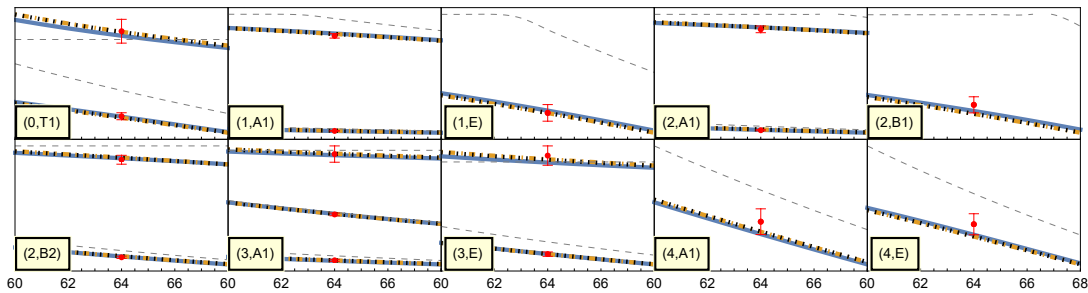


FIG. 1. Spectra with  $m_\pi = 200$  MeV provided by Bulava *et al.* [34] along with that calculated by HEFT using the fitting results for schemes A, B and C. The  $x$ -axis represents the spatial extent  $L$  in units of lattice spacing  $a$ , while the  $y$ -axis indicates the energy level. Tick marks on the  $y$ -axis are omitted for clarity. Text within the yellow box  $(\mathbf{n}^2, \Gamma)$  signifies spectrum extraction using operators in representation  $\Gamma$  and with total momentum  $\mathbf{P}^2 = (\frac{2\pi}{L})^2 \mathbf{n}^2$ . Red points indicate the lattice spectrum provided by collaborations. Blue, orange dot-dashed and black dotted lines indicate the spectrum as the function of  $L$  calculated by HEFT using the fitting results of schemes A, B and C, respectively. The dashed gray lines indicate the non-interacting energy levels  $2E_\pi(\mathbf{k}^*)$  and  $m_\rho^B$  (with  $m_\rho^B$  taken from Scheme A's fitting result for illustration). The turning points in the non-interacting energy levels are associated with energy crossings where the non-interacting two-particle energy becomes lower than the bare  $\rho$ -meson mass as  $L$  increases.

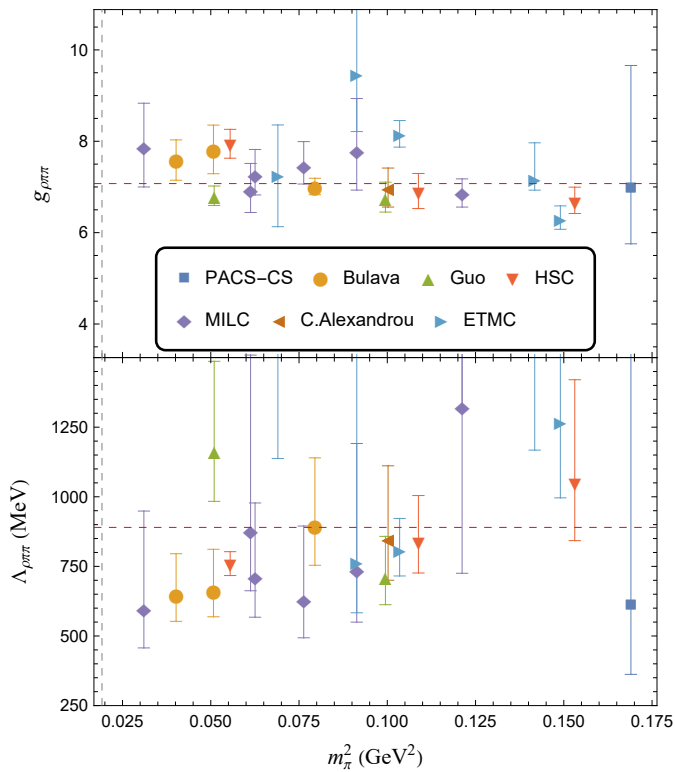


FIG. 2.  $m_\pi$ -dependence of  $g_{\rho\pi\pi}$  and  $\Lambda_{\rho\pi\pi}$  in scheme A. The dashed gray vertical line indicates the physical  $m_\pi$ . The dashed red horizontal lines indicate the value that will be fixed for  $N_f = 2 + 1$  in scheme B.

In contrast, the  $m_\pi$ -dependence of  $m_\rho^B$  suffers a large fluctuation, as illustrated in the top section of Fig. (3). This behavior stems from the limited number of energy levels available for each pion mass, coupled with the considerable uncertainties associated with  $g_{\rho\pi\pi}$  and  $\Lambda_{\rho\pi\pi}$ . In

order to reduce the uncertainty associated with the bare mass, one needs to find an appropriate method to combine the analysis of the various energy levels. Inspired by the weak dependence on  $m_\pi$ , as well as the sizable uncertainties of  $g_{\rho\pi\pi}$  and  $\Lambda_{\rho\pi\pi}$ , we choose these two parameters to be constant for all pion masses and re-fit each spectrum using only one single parameter,  $m_\rho^B$ .

## 2. Results for Scheme B

The first task is to determine the constant values of  $g_{\rho\pi\pi}$  and  $\Lambda_{\rho\pi\pi}$  which will be used in the analysis of the data for all values of  $m_\pi$ . To do that, we investigate  $m_\pi = 236, 280, 322, 376, 386, 391$  MeV cases, which have the highest values of the chi-squared per degree of freedom,  $\hat{\chi}^2 (= \chi^2/\text{dof})$ , in scheme A. We present the distribution of the sum of these  $\hat{\chi}^2$  with respect to some fixed  $g_{\rho\pi\pi}$  and  $\Lambda_{\rho\pi\pi}$  in Fig. 4. It is straightforward to find the preferred values of the coupling and cutoff from this distribution. It leads us to choose the values at the black point, where  $g_{\rho\pi\pi} = 7.07$  and  $\Lambda_{\rho\pi\pi} = 890$  MeV for  $N_f = 2 + 1$ . On the other hand, it is found that for  $N_f = 2$ , we should use slightly different values, namely  $g_{\rho\pi\pi} = 6.75$  and  $\Lambda_{\rho\pi\pi} = 950$  MeV [37, 38]. These values ensure the  $\hat{\chi}^2$  satisfies the condition  $\hat{\chi}^2 \lesssim 2$  for all of these values of  $m_\pi$ , as illustrated in Table III, in the column of  $\hat{\chi}^2$  for scheme B.

For scheme B, the curves denoting the spectra as a function of the spatial extent,  $L$ , are shown as orange dot-dashed lines in the figures in Appendix D. The fitted  $m_\rho^B$  values are presented in Fig. 3, and the columns for scheme B in Table III. Comparing Fig. 3(A) with (B), one finds that the uncertainties in  $m_\rho^B$  are significantly reduced, albeit with slight shifts in the central values. The  $m_\pi$ -dependence of  $m_\rho^B$  remains unclear. In particular, the values of  $m_\rho^B$  at  $m_\pi = 301, 302, 315, 316$

TABLE III. Fitting results of schemes A, B, and C provided by the MINUIT2 program [57]. In the columns for scheme A, we show asymmetric uncertainties, since in this scheme the upper and lower uncertainties are quite different. The question mark means that some upper uncertainties are not provided by MINUIT2 since even for a very large  $\Lambda_{\rho\pi\pi}$  the energy levels can still be fit well. For scheme B,  $g_{\rho\pi\pi}$ , and  $\Lambda_{\rho\pi\pi}$  are fixed at 7.07 (6.85) and 890 (950) MeV for  $N_f = 2 + 1$  (2), respectively. For scheme C,  $g_{\omega\rho\pi}$  and  $\Lambda_{\omega\rho\pi}$  are fixed at 18/GeV and 900 MeV, while  $g_{\rho\pi\pi}$  and  $\Lambda_{\rho\pi\pi}$  are fixed at 7.07 (6.85) and 900 (980) MeV for  $N_f = 2 + 1$  (2), respectively.  $\hat{\chi}^2$  represents the reduced chi-square, i.e.  $\chi^2/\text{dof}$  with  $\text{dof} = N_{\text{lvl}} - 3$  for scheme A and  $N_{\text{lvl}} - 1$  for schemes B and C.

COLLAB.(Year)	$m_\pi$ (MeV)	Scheme A				Scheme B		Scheme C	
		$m_\rho^{\text{B}}$ (MeV)	$g_{\rho\pi\pi}$	$\Lambda_{\rho\pi\pi}$ (MeV)	$\hat{\chi}^2$	$m_\rho^{\text{B}}$ (MeV)	$\hat{\chi}^2$	$m_\rho^{\text{B}}$ (MeV)	$\hat{\chi}^2$
J.Bulava(2018)	200	787.3 <sup>+23.6</sup> <sub>-14.8</sub>	7.58 <sup>+0.45</sup> <sub>-0.43</sub>	645.6 <sup>+149.8</sup> <sub>-93.0</sub>	0.44	819.6(4.1)	0.53	867.7(4.5)	0.53
	220	795.0 <sup>+18.6</sup> <sub>-11.5</sub>	7.80 <sup>+0.55</sup> <sub>-0.51</sub>	662.0 <sup>+149.4</sup> <sub>-93.0</sub>	0.41	818.4(3.6)	0.49	866.3(4.0)	0.50
	280	825.1 <sup>+29.4</sup> <sub>-14.7</sub>	7.00 <sup>+0.19</sup> <sub>-0.17</sub>	895.7 <sup>+244.1</sup> <sub>-141.7</sub>	1.07	826.2(2.4)	0.93	870.8(2.6)	0.97
HSC(2013)	391	909.0 <sup>+36.4</sup> <sub>-15.5</sub>	6.66 <sup>+0.33</sup> <sub>-0.24</sub>	1050.3 <sup>+370.1</sup> <sub>-207.8</sub>	0.98	898.9(1.2)	0.97	936.2(1.3)	1.21
HSC(2015)	236	829.1 <sup>+29.4</sup> <sub>-14.7</sub>	7.94 <sup>+0.32</sup> <sub>-0.31</sub>	756.4 <sup>+46.4</sup> <sub>-39.3</sub>	1.00	840.3(1.0)	1.38	888.6(1.1)	1.62
HSC(2023)	330	856.1 <sup>+13.1</sup> <sub>-8.2</sub>	6.89 <sup>+0.41</sup> <sub>-0.36</sub>	838.6 <sup>+165.9</sup> <sub>-112.3</sub>	0.71	862.6(2.2)	0.78	904.1(2.4)	0.86
MILC(2016)	176	806.4 <sup>+36.3</sup> <sub>-8.5</sub>	7.88 <sup>+0.96</sup> <sub>-0.88</sub>	596.2 <sup>+352.5</sup> <sub>-139.1</sub>	0.63	831.7(8.2)	0.61	882.9(9.1)	1.30
	247	878.2 <sup>+84.1</sup> <sub>-21.2</sub>	6.93 <sup>+0.58</sup> <sub>-0.49</sub>	876.0 <sup>+633.0</sup> <sub>-213.5</sub>	0.73	881.3(3.9)	0.57	928.7(4.3)	0.53
	248	855.8 <sup>+28.6</sup> <sub>-12.4</sub>	7.27 <sup>+0.55</sup> <sub>-0.44</sub>	711.7 <sup>+266.1</sup> <sub>-144.3</sub>	0.37	874.3(4.1)	0.35	921.5(4.5)	0.32
	275	861.5 <sup>+29.1</sup> <sub>-12.5</sub>	7.45 <sup>+0.54</sup> <sub>-0.39</sub>	630.2 <sup>+264.7</sup> <sub>-136.7</sub>	0.36	886.0(5.5)	0.43	932.4(6.0)	0.41
	301	916.6 <sup>+47.2</sup> <sub>-13.8</sub>	7.79 <sup>+1.15</sup> <sub>-0.86</sub>	735.8 <sup>+455.7</sup> <sub>-186.0</sub>	0.26	928.5(5.8)	0.29	972.4(6.4)	0.28
	346	999.8 <sup>+?</sup> <sub>-51.9</sub>	6.86 <sup>+0.31</sup> <sub>-0.30</sub>	1321.0 <sup>+?</sup> <sub>-595.8</sub>	0.26	958.9(6.4)	0.23	998.6(6.9)	0.28
ETMC(2020)	322	927.4 <sup>+14.4</sup> <sub>-10.6</sub>	8.15 <sup>+0.30</sup> <sub>-0.28</sub>	807.2 <sup>+115.0</sup> <sub>-91.6</sub>	1.20	924.4(2.6)	2.16	967.6(2.8)	2.06
	386	999.6 <sup>+59.5</sup> <sub>-21.8</sub>	6.30 <sup>+0.28</sup> <sub>-0.23</sub>	1267.3 <sup>+557.2</sup> <sub>-271.1</sub>	1.32	974.1(2.2)	1.54	1012.1(2.4)	2.00
	262	1156.2 <sup>+68.7</sup> <sub>-208.0</sub>	7.26 <sup>+1.10</sup> <sub>-1.13</sub>	2421.0 <sup>+?</sup> <sub>-1283.4</sub>	0.58	920.2(8.6)	0.67	967.3(9.5)	0.72
	302	928.7 <sup>+157.1</sup> <sub>-23.7</sub>	9.46 <sup>+1.42</sup> <sub>-1.25</sub>	765.6 <sup>+862.6</sup> <sub>-182.3</sub>	0.56	919.1(5.8)	1.00	964.8(6.3)	0.99
	376	1034.6 <sup>+170.3</sup> <sub>-51.8</sub>	7.16 <sup>+0.81</sup> <sub>-0.23</sub>	1571.4 <sup>+?</sup> <sub>-403.8</sub>	0.98	952.6(1.8)	1.57	993.4(1.9)	1.52
C.Alexandru(2017)	316	840.6 <sup>+25.8</sup> <sub>-12.7</sub>	6.96 <sup>+0.45</sup> <sub>-0.40</sub>	847.4 <sup>+263.9</sup> <sub>-147.1</sub>	0.10	846.6(2.3)	0.10	890.1(2.5)	0.10
PACS-CS(2011)	411	913.0 <sup>+185.0</sup> <sub>-10.2</sub>	6.97 <sup>+2.70</sup> <sub>-1.21</sub>	609.0 <sup>+?</sup> <sub>-246.8</sub>	0.83	934.3(5.2)	0.82	973.3(5.6)	0.88
Guo(2016)	226	834.4 <sup>+43.7</sup> <sub>-21.3</sub>	6.79 <sup>+0.23</sup> <sub>-0.19</sub>	1163.1 <sup>+323.4</sup> <sub>-179.6</sub>	1.69	854.3(1.4)	1.88	806.4(1.3)	1.78
	315	824.1 <sup>+11.6</sup> <sub>-7.0</sub>	6.75 <sup>+0.35</sup> <sub>-0.30</sub>	709.5 <sup>+148.2</sup> <sub>-97.1</sub>	0.20	892.4(1.4)	1.50	848.0(1.3)	1.84

and 322 MeV extracted from MILC, ETMC, Guo *et al.*, C. Alexandru *et al.*, and ETMC respectively, significantly fluctuate between 840 and 920 MeV. It is apparent that there are substantial differences in the results from different LQCD groups. To address this issue, we examine the contribution of the coupling to the  $\omega\pi$  [51, 55] channel, which is the closest two-particle channel in the present work and which, significantly, yields the leading non-analytic contribution to the  $\rho$  self-energy.

### 3. Results for Scheme C

Once  $V_{\omega\pi}$  is turned on, two additional parameters,  $g_{\omega\rho\pi}$  and  $\Lambda_{\omega\rho\pi}$ , are involved. In addition,  $m_\omega$  also depends on  $m_\pi$ . Since  $m_\omega$  is not commonly provided by LQCD collaborations, we set it equal to the function  $m_\rho^{\text{B}}$  found in scheme B, as the experimental values of  $m_\rho$  and  $m_\omega$  are almost the same. Since the threshold of  $\omega\pi$  is higher than the spectrum extracted, it is expected that the  $\omega\pi$  loop will shift the value of  $m_\rho^{\text{B}}$  but have a negligible influence on the resulting  $\chi^2$ .

Instead of allowing  $g_{\omega\rho\pi}$  and  $\Lambda_{\omega\rho\pi}$  to be two additional free parameters, we impose appropriate constraints to fix

them. Two constraints are identified at the physical pion mass  $\mu_\pi$ : the decay width,  $\Gamma_{\omega\rightarrow 3\pi}$ , is primarily determined by the  $\omega \rightarrow \rho\pi \rightarrow 3\pi$  mechanism (which is estimated to yield around 90% [59] of the width) and the  $P$ -wave phase shifts of  $\pi\pi \rightarrow \pi\pi$  in the energy region around the  $\rho$  mass.

For simplification, we take the two cut-off,  $\Lambda_{\rho\pi\pi}$  and  $\Lambda_{\omega\rho\pi}$ , to share the same value. Consequently, there are four undetermined parameters left, namely two coupling constants, one cut-off and one bare mass. Once  $g_{\rho\pi\pi}$  and  $\Lambda_{\rho\pi\pi}$  are fixed, the other parameters at  $\mu_\pi$  can also be determined from the decay width of  $\omega \rightarrow 3\pi$  and the  $P$ -wave phase shifts of  $\pi\pi \rightarrow \pi\pi$  at the physical pion mass  $\mu_\pi$ .

The detailed procedure for parameter determination is presented in Appendix B. Here, we simply summarize the preferred values:  $g_{\rho\pi\pi} = 7.07$  (6.75) and  $\Lambda_{\omega\rho\pi} = \Lambda_{\rho\pi\pi} = 900$  (980) MeV for  $N_f = 2 + 1$  ( $N_f = 2$ ) and  $g_{\omega\rho\pi} = 18/\text{GeV}$  for either  $N_f$ . It is worth mentioning that our value of  $g_{\omega\rho\pi}$  is similar to that used in Ref. [51], 16/GeV. Additionally,  $g_{\rho\pi\pi}$  and  $\Lambda_{\omega\rho\pi}$  are slightly shifted compared to those found using scheme B, because of the introduction of the  $\omega\pi$  channel. We then proceed to minimize the total  $\chi^2$  by fitting the value of  $m_\rho^{\text{B}}$  for each pion



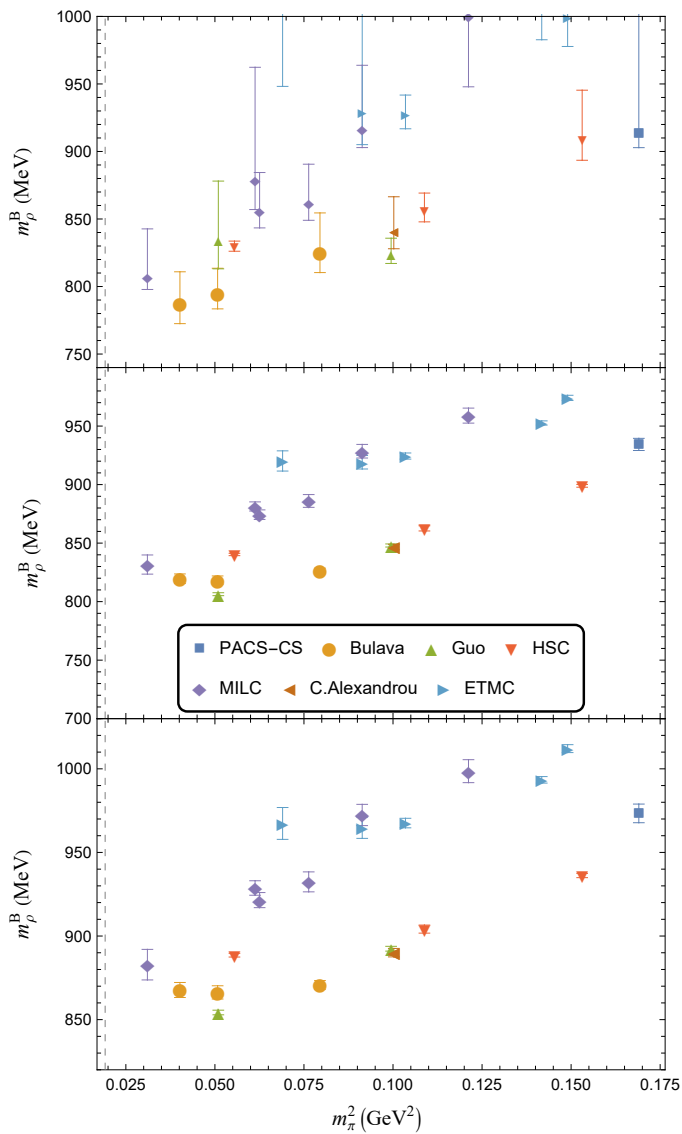


FIG. 3.  $m_\pi$ -dependence of  $m_\rho^B$  in schemes A, B and C from top to bottom. The dashed gray vertical line indicates the physical  $m_\pi$  value.

mass.

The fitted spectra as functions of the spatial extent,  $L$ , for scheme C are shown as black dotted lines in the figures of Appendix D, which illustrates only minor discrepancies from the orange dot-dashed lines found using scheme B, as expected. The fitted values of  $m_\rho^B$  are presented in the lower portion of Fig. 3 and are tabulated in the columns for scheme C in Table III. The preferred values of  $m_\rho^B$  are about 50 MeV higher than found in scheme B because of the additional self-energy term,  $\Sigma_{\omega\pi}$ , as defined in Eq. (17).

Even after including the effect of the  $\omega\pi$  coupled channel, the  $m_\pi$ -dependence of  $m_\rho^B$  shown in Fig.3 is still scattered. It becomes apparent that the bare masses extracted from different lattice groups do not permit a con-

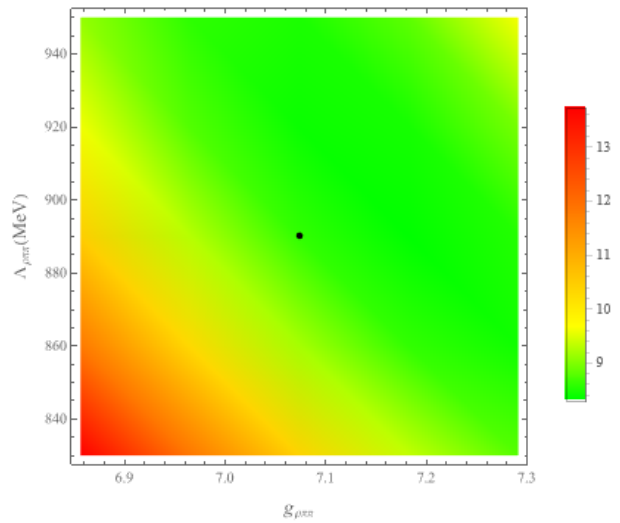


FIG. 4. Distribution of  $\sum_{m_\pi \in S} \hat{\chi}^2(m_\pi)$  for scheme B using fixed values of  $(g_{\rho\pi\pi}$  and  $\Lambda_{\rho\pi\pi})$ , where  $S = \{301, 302, 315, 316, 322\}$ . Using the black point marked in the green region ensures that  $\hat{\chi}^2(m_\pi) \lesssim 2$  is satisfied for each value of  $m_\pi \in S$ .

sistent interpretation, which indicates the presence of intrinsic systematic differences between the lattice spectra provided by different collaborations. Such discrepancies lead us to consider the following issues that may influence the lattice results presented. These include:

- Different residual lattice artefacts due to the different gauge and fermion actions considered.
- Varied scale-setting schemes employed by different collaborations.
- Different methods used to extract the finite volume spectra.

In the absence of systematic errors, the results provided by different collaborations should be consistent with each other after finite volume and lattice spacing artefacts are taken into account. Our HEFT approach enables one to account for the finite volume of the lattice, several values of the pion mass, as well as lattice spacing artefacts, all within a single formalism. As such, this is the first examination of the self consistency of world lattice QCD results for  $\pi\pi$  scattering in  $\rho$  meson channel.

#### D. Extrapolation in $m_\pi$

In the last section, we present the outcomes of our fitting approach applied to the finite volume spectra provided by various collaborations for a wide range of values of  $m_\pi$ . With these results, we now investigate the  $m_\pi$ -dependence of the properties of the  $\rho$  meson and extrapolate them into the physical region. In scheme A, our investigations reveal that both  $g_{\rho\pi\pi}$  and  $\Lambda_{\rho\pi\pi}$  display little variation as  $m_\pi$  varies. In the spirit of chiral

TABLE IV. Extrapolation results are summarized for schemes B and C. For each collaboration, the results of B and C are given in the first and second row, respectively. The second and third column present the coefficient  $c_0$  and  $c_1$  defined in Eq.(40). The fourth column presents the extrapolated  $m_\rho^B$  at the physical pion mass. The fifth column presents the pole mass, defined by Eq.(20).

COLLAB.	$c_0(\text{MeV})$	$c_1(\text{GeV}^{-1})$	$m_\rho^B(\mu_\pi)$	$m_\rho^P(\mu_\pi)$
Bulava	809.8(7.0)	0.21(0.11)	814.0(5.0)	765.0(6.0)
	862.3(7.6)	0.11(0.12)	864.0(6.0)	765.0(6.0)
MILC	788.0(7.3)	1.45(0.10)	816.0(6.0)	768.0(6.0)
	843.3(7.95)	1.32(0.11)	869.0(6.0)	769.0(6.0)
HSC	806.7(1.71)	0.60(0.02)	818.2(1.4)	770.6(1.7)
	861.3(1.9)	0.49(0.02)	870.7(1.6)	771.3(1.7)
ETMC	838.9(7.7)	0.85(0.06)	855.0(7.0)	814.0(8.0)
	892.5(8.3)	0.75(0.06)	907.0(7.0)	809.0(7.0)
Guo	762.2(2.9)	0.86(0.04)	778.8(2.3)	719.3(2.6)
	813.8(3.2)	0.79(0.04)	829.0(2.5)	719.0(2.6)

effective field theory, the couplings and regulator parameters are held fixed. Thus, we could concentrate on the  $m_\pi$ -dependence of the bare  $\rho$  mass,  $m_\rho^B$ , using Eq. (40). It is possible to extrapolate the fitting results of  $m_\rho^B$  in schemes B and C, but not in scheme A, since there the values of  $m_\rho^B$  are correlated with  $g_{\rho\pi\pi}$  and  $\Lambda_{\rho\pi\pi}$ .

In principle, it is natural to consider putting all the values of  $m_\rho^B(m_\pi)$  together and performing a global fit to make full use of the lattice data. However, from the two lower figures in Fig. 3, it is hard to extract useful information, since the data show large inconsistent variations. The possible reasons have been discussed in the previous section.

For example, with reference to the discussion about the lattice spacing effect in Eq. (41), the coefficient  $\xi$  can be different for each LQCD group. In practice, we tried to use Eq. (41), with a single value of  $\xi$  to do the extrapolation but that fitting process yields a large  $\chi^2$ . Also, there is a huge difference between the values of observables calculated using the parameters extrapolated to physical  $m_\pi$  and those measured in experiments. This suggests that we should make the extrapolation of the data to the physical point collaboration by collaboration.

Because for each group, there are only a limited number of values of  $m_\pi$  and the lattice spacing does not change a lot, we neglect the lattice spacing term and just use Eq. (40) to perform the extrapolations. Furthermore, we have two free parameters in Eq. (40), thus only the data of collaborations having no less than two  $m_\pi$  points are analyzed. The fitting and extrapolation results are shown in Fig. 5 and Table IV.

As shown in Fig. 5, there are five collaborations having no less than two different  $m_\pi$  points. For each collaboration, the points show a good linear relation between  $m_\rho^B$

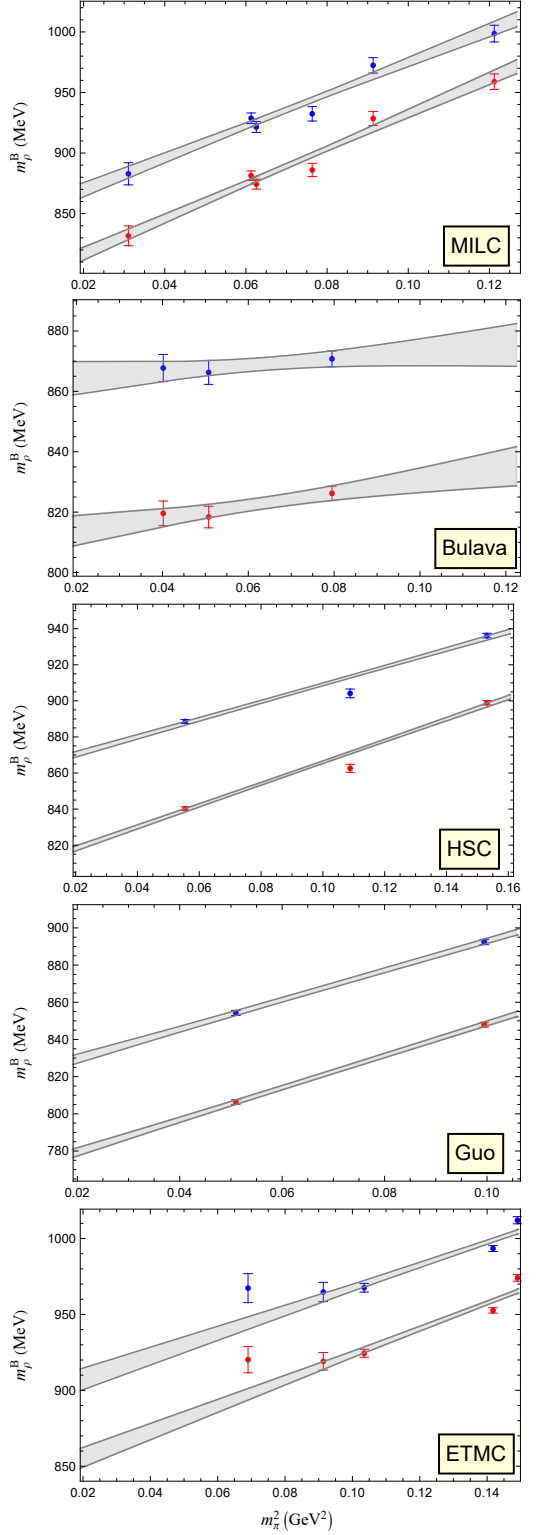


FIG. 5.  $m_\pi$ -dependence and extrapolation of  $m_\rho^B$  for each collaboration. Red and blue points indicate the fitting results of  $m_\rho^B$  in schemes B and C, respectively. Gray bands represent the quadratic function  $m_\rho^B = c_0 + c_1 m_\pi^2$  with uncertainty, where  $c_0$  and  $c_1$  for both schemes are given in Table IV. For convenience the lower bound of the  $m_\pi^2$ -axis is set as the physical value  $\mu_\pi^2$ .

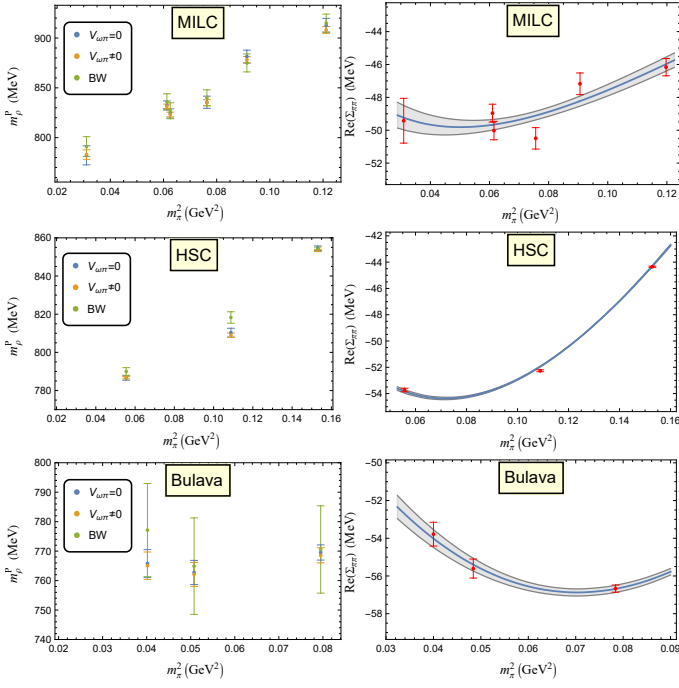


FIG. 6.  $m_\pi$ -dependence of  $m_\rho^p$  and the real part of the self-energy  $\Sigma_{\pi\pi}$ . Left column:  $m_\rho^p$  defined by Eq.(20) using parameters for schemes B and C, and  $m_\rho$  obtained from the Breit-Wigner parameterization of the phase shift provided in each paper. Right column: real part of the self-energy  $\Sigma_{\pi\pi}$ . Blue lines with gray bands represent the  $\text{Re}\Sigma_{\pi\pi}(m_\rho^p) \approx m_\rho^p(m_\rho^B) - m_\rho^B$  as in Eq.(39) using  $m_\rho^B = c_0 + c_1 m_\pi^2$  with  $c_0$  and  $c_1$  being the extrapolation coefficients for scheme B presented in Table IV. Red points also represent  $\text{Re}\Sigma_{\pi\pi}$  but using  $m_\rho^B$  from fitting results of scheme B presented in Table III.

and  $m_\pi^2$ , whether the  $\omega\pi$  loop is included or not. The only notable exception is one point with a large uncertainty from ETMC. With  $c_0$  and  $c_1$  determined, we can obtain the bare mass of the  $\rho$  at the physical pion mass. Subsequently, we can get the physical  $\rho$  mass by solving Eq. (20). The results are listed in the last column of Table IV.

For MILC, HSC and Bulava *et al.*, even though their values of  $c_0$  and  $c_1$  are quite different, the extrapolated  $m_\rho^p$  all agree with the experimental value. However, for ETMC and Guo *et al.*, they are about 30 MeV higher and 50 MeV lower compared to the experimental value, respectively. The relatively high  $m_\rho^p$  obtained by ETMC is not so surprising, since in their previous work [31] a higher value of  $m_\rho$  compared to the others was also reported. The lower  $m_\rho^p$  extracted from Guo *et al.* also agrees with their own result, presented in Ref. [32], which possibly results from using  $N_f = 2$ . Clearly, the physical  $\rho$  masses obtained here all indicate the consistency between our method and previous work, while in addition we provide detailed information on the  $m_\pi$ -dependence of  $m_\rho^B$ .

## E. Discussion and Exploration

In this section, we make some remarks concerning the numerical results. In scheme A, we first found that the coupling constants  $g_{\rho\pi\pi}$  and cut-off  $\Lambda_{\rho\pi\pi}$  are both weakly dependent on  $m_\pi$ . This conclusion supports our previous study of the baryon resonances,  $\Lambda(1405)$ ,  $N^*(1535)$  and  $N^*(1440)$  (Roper), where we only considered the  $m_\pi$  dependence of the masses of various hadrons but not the couplings and cut-off. Furthermore, the large uncertainty found for the cut-off is also acceptable, because in principle the physical observables should not be so sensitive to it.

In Eq. (38), there are many nonlinear terms in  $m_\pi^2$ , arising from the self-energy part. In the right column of Fig. 6, we show the value of the  $\text{Re}\Sigma_{\pi\pi}$  at the pole position as a function of  $m_\pi^2$ . Given  $m_\rho^B$ ,  $\text{Re}\Sigma_{\pi\pi}$  is calculated by  $m_\rho^p - m_\rho^B$  as in Eq. (39), where  $m_\rho^p$  is obtained from Eq. (20). Scalars in the figure are calculated by using the values of  $m_\rho^B$  from the fitting results of scheme B presented in Table III, while the lines with error bands use  $m_\rho^B = c_0 + c_1 m_\pi^2$ , with  $c_0$  and  $c_1$  being the coefficients for scheme B presented in Table IV.

Clearly both these scalars and lines in Fig. 6 exhibit a nonlinear behavior. However, the difference of  $\text{Re}\Sigma_{\pi\pi}$  at different  $m_\pi$  are just around 10 MeV when  $m_\pi$  varies over the range 140 to 400 MeV. Therefore, there will also be an approximately linear relation between  $m_\rho^p$  and  $m_\pi^2$ , as shown in the left column of Fig. 6, where the Breit-Wigner masses provided by the three collaborations are also shown. This is the reason why the Breit-Wigner  $\rho$  mass could be described well by a linear function of  $m_\pi^2$  in Ref. [33].

Things are similar even when the  $\omega\pi$  channel is introduced. From Table IV one can see that  $m_\rho^p$  is nearly unchanged while  $m_\rho^B$  changes a lot when  $V_{\omega\pi}$  turns on. Nonetheless,  $m_\rho^B$  still exhibits a linear relation to  $m_\pi^2$  as shown in Fig. 5, where the two lines are almost parallel for each LQCD group. Also, it is apparent that the contribution from the  $\omega\pi$  loop only makes a significant change in the value of  $c_0$ , but just slightly modifies the slope,  $c_1$ . These facts suggest that  $\text{Re}\Sigma_{\omega\pi}$  is also weakly dependent on  $m_\pi$  and its effect can be effectively absorbed into  $c_0$ .

In summary, the slow variation of the contributions from  $\pi\pi$  and  $\omega\pi$  loops significantly affects  $c_0$ , while only slightly influencing the slope,  $c_1$ . Therefore, it makes little sense to talk about  $m_\rho^B$  solely based on experimental results, as the fitted  $m_\rho^B$  strongly depends on how the hadronic loops are estimated. It is the slope  $c_1$  that contains more useful, less model dependent, physical information concerning the structure of the  $\rho$  meson, which can only be extracted from the LQCD data at unphysical  $m_\pi$ . Furthermore, in principle, on the theoretical side the slope  $c_1$  can be calculated at the quark-level in various models. Thus, with the help of  $c_1$  the relevant models could be distinguished. This is quite a good example of the idea that the data extracted at unphysical values of

TABLE V. Composition of eigenstates  $|\psi\rangle$  of some energy levels from HSC(2015). In the first column,  $|\psi\rangle$  is labelled by  $(\mathbf{n}^2, \Gamma)$ , as it is the eigenstate that has the largest  $\rho_B$  component among those whose energies are extracted by the operators in representation  $\Gamma$  and with total momentum  $\mathbf{P}^2 = (\frac{2\pi}{L})^2 \mathbf{n}^2$ , as shown in Fig. 16. In the subsequent column we present the composition of  $|\psi\rangle$ , i.e.  $|\langle\phi|\psi\rangle|^2$  with  $|\phi\rangle = |\rho_B\rangle, |\pi\pi\rangle$  for  $V_{\omega\pi} = 0$  and also  $|\omega\pi\rangle$  for  $V_{\omega\pi} \neq 0$ .

$(\mathbf{n}^2, \Gamma)$	$V_{\omega\pi} = 0$		$V_{\omega\pi} \neq 0$		
	$\rho_B$	$\pi\pi$	$\rho_B$	$\pi\pi$	$\omega\pi$
$(1, A_1)$	0.7365	0.2635	0.6966	0.2664	0.0370
$(2, A_1)$	0.7963	0.2037	0.7537	0.2028	0.0434
$(3, A_1)$	0.7701	0.2299	0.7295	0.2241	0.0464
$(4, A_1)$	0.7432	0.2568	0.7093	0.2503	0.0404
$(3, E)$	0.6514	0.3486	0.6171	0.3394	0.0434

$m_\pi$  are able to provide us with additional information concerning the structure of hadrons.

The linear relation between  $m_\rho^B$  and  $m_\pi^2$  is consistent with the assumption that  $|\rho_B\rangle$  is a pure  $q\bar{q}$  state. Additionally, the contribution from hadron loops to  $m_\rho^P$  accounts for only approximately 20% of the total mass for the optimal value of the regulator parameter. Consequently, we can also conclude that the bare  $\rho$  plays the most important role in the structure of the observed  $\rho$  meson. To confirm this, we pick out several eigenstates whose energy is close to the physical  $\rho$  mass and look at their composition, a feature which is characteristic of HEFT. The eigenstates of the FVH are the counterpart in the finite volume of continuous scattering states in the infinite volume [43]. Therefore, obviously, it is expected that the eigenstate whose energy is closest to the resonance region is the counterpart of the  $\rho$ . For illustration, we pick five eigenstates from the spectrum generated by HSC(2015) with  $m_\pi = 236$  MeV and calculate the probabilities of the bare state,  $\pi\pi$  and  $\omega\pi$  components. The results are presented in Table V. It is found that the component  $\rho_B$  has a probability around 75%. That is, it is definitely dominant.

With the parameters listed in Table III, we can predict the  $\pi\pi \rightarrow \pi\pi$   $P$ -wave phase shift at unphysical masses. Here we focus on the three collaborations whose values of  $m_\rho^P$  at the physical  $m_\pi$  agree with the experimental value. In Fig. 7, we show the phase shifts calculated for four different values of  $m_\pi$ . In the first row, at the physical point, the phase shifts of the three collaborations are nearly the same. This is expected since their values of  $m_\rho^B$  at physical  $m_\pi$  are consistent. They are in good agreement with the experimental data, except for the region away from resonance, where the  $\pi\pi - \pi\pi$   $t/u$ -channel interaction may not be negligible.

In other rows we predict the phase shifts of the three collaborations at three unphysical values of  $m_\pi$ . Since the values of  $c_0$  and  $c_1$  obtained by analysis of the data

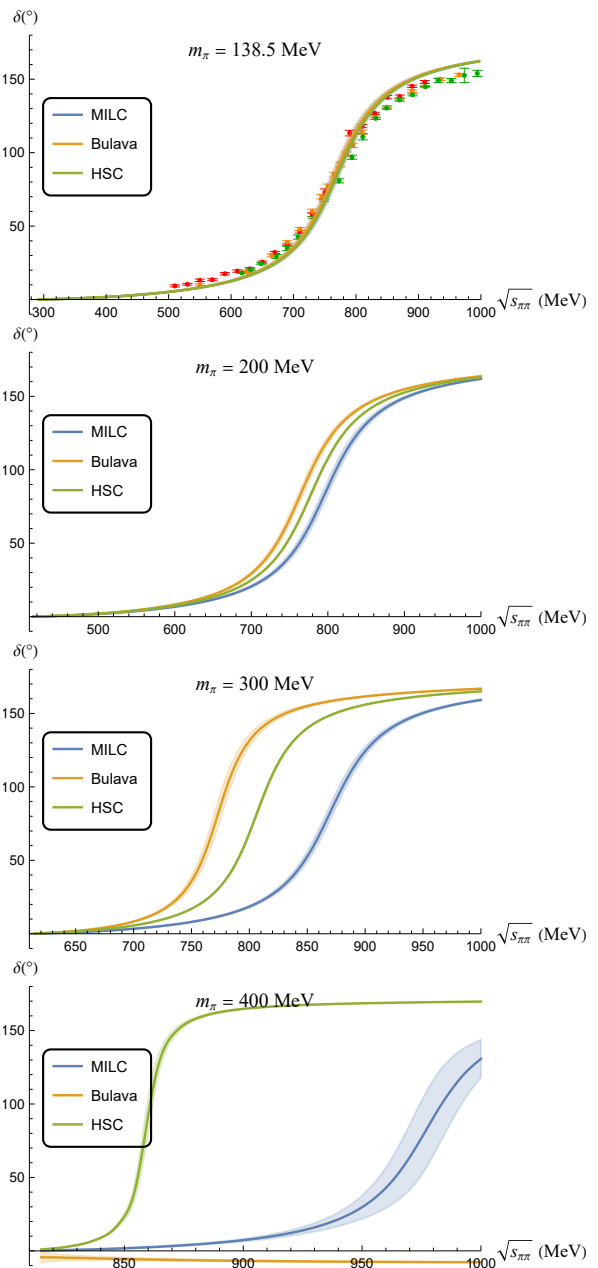


FIG. 7. Phase shift calculated by Eq. (19) using the parameters  $g_{\omega\rho\pi} = 0$ ,  $g_{\rho\pi\pi} = 7.07$ ,  $\Lambda_{\rho\pi\pi} = 890$  MeV and  $m_\rho = c_0 + c_1 m_\pi^2$  with  $c_0$  and  $c_1$  being the extrapolation coefficients for scheme B given in Table IV. The points in the first figure are experimental values from Ref. [60–62]. The line for Bulava at  $m_\pi = 400$  MeV denotes a  $\pi\pi$  bound state.

from these three collaborations are very different, their phase shifts are not consistent. Especially, for  $m_\pi = 400$  MeV, we predict that the typical line shape would disappear in the phase shifts of  $\pi\pi$  scattering for Bulava *et al.*, since it would be a bound state of  $\pi\pi$ .

The most serious problem found in this work is that the two coefficients,  $c_0$  and  $c_1$ , differ a lot for different LQCD groups. This unexpected variation arises from dif-

ferences in the lattice QCD simulations, the interpolating fields considered in constructing correlation matrices, the analysis methods applied to the correlation matrices and finally the scale-setting schemes.

The use of different  $\mathcal{O}(a)$ -improved actions gives rise to different  $\mathcal{O}(a^2)$  errors such that the coefficient of  $a^2$  differs for each set of lattice QCD results. It will be important to have two or more different lattice spacings available in high-quality sets to enable a determination and elimination of this lattice artefact.

State isolation is key to measuring the subtle shifts of the finite-volume energies from their non-interacting energies, vital to measuring a phase shift. In obtaining consistency across lattice collaborations, modern projected correlator methods should be adopted to reduce excited state contamination in the extracted energy eigenvalues. Moreover, all nonlocal two particle momentum-projected interpolating fields participating in the resonance region need to be considered and mixed with the single particle operators to ensure multiple eigenstates are not participating in the state-projected correlation functions of the correlation matrix. In the present case, single particle  $\rho$  interpolations are to be mixed, not only with  $\pi\pi$  correlations, but also with  $\pi\omega$  correlators. Indeed, Fig. 1 and the figures in Appendix.D, illustrating the fits of HEFT to contemporary lattice QCD results, raise concerns about multi-state contamination in the analysis.

Finally, the choice of scale setting scheme is of vital importance when attempting to describe QCD properties away from the physical point. While all schemes are designed to extrapolate to the physical point, the manner in which they move away from the physical point is different. The Sommer scale is designed to be physical. Maintaining physics at the scale relevant to the charmonium spectrum, it naturally includes changes in the renormalization of the strong coupling constant due to changes in the sea quark masses. However, other schemes where the quark mass has no effect on the coupling constant are possible, provided the only goal is to get to the physical point. In light of the plethora of scale setting schemes currently proposed, we encourage the consideration of how well a proposed scheme is suited to learning the properties of QCD in a universe with different quark masses.

#### IV. SUMMARY AND OUTLOOK

In this work, we collected finite volume spectra for the  $I = \ell = 1$   $\pi\pi$  sector provided by LQCD collaborations over the past decade. These spectra were fit in a consistent manner within the framework of Hamiltonian Effective field theory. The basic states included in the Hamiltonian were a bare  $\rho$  state and the  $\pi\pi$  and  $\omega\pi$  coupled channels. In this framework, we successfully fit the finite volume spectra in the rest frame, moving frame and the elongated box, and complemented this with experimental data for the  $\pi\pi \rightarrow \pi\pi$   $P$ -wave phase shifts.

We employed three schemes to fit the energy levels obtained at various pion masses. Through scheme A, we found that  $g_{\rho\pi\pi}$  and  $\Lambda_{\rho\pi\pi}$  exhibit a weak dependence on  $m_\pi$ . In the following scheme B, we set these two parameters as constant in order to obtain the  $m_\pi$ -dependence of the bare  $\rho$  basis state,  $m_\rho^B(m_\pi)$ . In scheme C, where the  $\omega\rho\pi$  vertex was included with additional constraints from experimental data, we again extracted  $m_\rho^B(m_\pi)$ . Finally, we used the linear relation between  $m_\rho^B$  and  $m_\pi^2$ , as shown in Eq. (38), to perform an extrapolation. Because the relationship between  $m_\rho^B$  and  $m_\pi^2$  was highly dependent on the LQCD group whose data we used, we were unable to fit all  $m_\rho^B$  simultaneously, and resorted to extrapolating collaboration by collaboration.

Based upon the extrapolations of data from the five LQCD groups, it was found that for each collaboration,  $m_\rho^B(m_\pi)$  could be described well by Eq. (40). This supports the hypothesis that the single-particle bare  $\rho$  meson plays an important role in forming a physical peak in the  $P$ -wave  $\pi\pi$  scattering. For each group, the physical  $\rho$  mass and the coefficients  $c_1$  in Eq. (40) were stable with and without the  $\omega\pi$  loop contribution, while the bare mass had a shift of around 50 MeV. This implies that the value of  $c_1$  can be deduced from data at unphysical pion masses and is therefore well suited to distinguish different models. Unfortunately, from the current LQCD data, the extracted value of  $c_1$  is dependent on the lattice collaboration whose data is used. In the future it would obviously be ideal to have lattice data for the  $\rho$  meson at different pion masses with all systematic effects carefully controlled in order to study the  $m_\pi$ -dependence.

#### ACKNOWLEDGMENTS

We acknowledge useful discussions and valuable comments from Xu Feng, Feng-Kun Guo, Chuan Liu, Li-uming Liu, Guang-Juan Wang, Mao-Jun Yan, Yi-Bo Yang, Zhi Yang, Bing-Song Zou. This work was partly supported by the National Natural Science Foundation of China (NSFC) under Grants Nos. 12175239 and 12221005 (J.J.W), and by the National Key R&D Program of China under Contract No. 2020YFA0406400 (J.J.W), and by the Chinese Academy of Sciences under Grant No. YSBR-101 (J.J.W). This research was also undertaken with assistance of resources from the National Computational Infrastructure(NCI), provided through the National Computational Merit Allocation Scheme. This work was supported by the Australian Research Council through Discovery Projects DP190102215 and DP210103706 (DBL) and DP230101791 (AWT). Y. L. is supported by the Excellence Hub project "Unraveling the 3D parton structure of the nucleon with lattice QCD (3D-nucleon)" id EXCELLENCE/0421/0043 co-financed by the European Regional Development Fund and the Republic of Cyprus through the Research and Innovation Foundation. Y. L. further acknowledges computing time granted on Piz Daint at Centro Svizzero di

Calcolo Scientifico (CSCS) via the project with id s1174, JUWELS Booster at the Jülich Supercomputing Centre (JSC) via the project with id pines, and Cyclone at the

Cyprus institute (CYI) via the project with ids P061, P146 and pro22a10951.

- 
- [1] S. Capstick and W. Roberts, Quark models of baryon masses and decays, *Prog. Part. Nucl. Phys.* **45**, S241 (2000), arXiv:nucl-th/0008028.
- [2] T. A. DeGrand, R. L. Jaffe, K. Johnson, and J. E. Kiskis, Masses and Other Parameters of the Light Hadrons, *Phys. Rev. D* **12**, 2060 (1975).
- [3] S. Theberge, A. W. Thomas, and G. A. Miller, The Cloudy Bag Model. 1. The (3,3) Resonance, *Phys. Rev. D* **22**, 2838 (1980), [Erratum: *Phys.Rev.D* 23, 2106 (1981)].
- [4] A. W. Thomas, S. Theberge, and G. A. Miller, The Cloudy Bag Model of the Nucleon, *Phys. Rev. D* **24**, 216 (1981).
- [5] C. D. Roberts and A. G. Williams, Dyson-Schwinger equations and their application to hadronic physics, *Prog. Part. Nucl. Phys.* **33**, 477 (1994), arXiv:hep-ph/9403224.
- [6] F.-K. Guo, C. Hanhart, U.-G. Meißner, Q. Wang, Q. Zhao, and B.-S. Zou, Hadronic molecules, *Rev. Mod. Phys.* **90**, 015004 (2018), [Erratum: *Rev.Mod.Phys.* 94, 029901 (2022)], arXiv:1705.00141 [hep-ph].
- [7] C. A. Meyer and E. S. Swanson, Hybrid Mesons, *Prog. Part. Nucl. Phys.* **82**, 21 (2015), arXiv:1502.07276 [hep-ph].
- [8] A. W. Thomas, Chiral extrapolation of hadronic observables, *Nucl. Phys. B Proc. Suppl.* **119**, 50 (2003), arXiv:hep-lat/0208023.
- [9] M. Luscher, Two particle states on a torus and their relation to the scattering matrix, *Nucl. Phys. B* **354**, 531 (1991).
- [10] C. h. Kim, C. T. Sachrajda, and S. R. Sharpe, Finite-volume effects for two-hadron states in moving frames, *Nucl. Phys. B* **727**, 218 (2005), arXiv:hep-lat/0507006.
- [11] M. T. Hansen and S. R. Sharpe, Multiple-channel generalization of Lellouch-Lüscher formula, *Phys. Rev. D* **86**, 016007 (2012), arXiv:1204.0826 [hep-lat].
- [12] S. He, X. Feng, and C. Liu, Two particle states and the S-matrix elements in multi-channel scattering, *JHEP* **07**, 011, arXiv:hep-lat/0504019.
- [13] K. Rummukainen and S. A. Gottlieb, Resonance scattering phase shifts on a nonrest frame lattice, *Nucl. Phys. B* **450**, 397 (1995), arXiv:hep-lat/9503028.
- [14] M. Gockeler, R. Horsley, M. Lage, U. G. Meissner, P. E. L. Rakow, A. Rusetsky, G. Schierholz, and J. M. Zanotti, Scattering phases for meson and baryon resonances on general moving-frame lattices, *Phys. Rev. D* **86**, 094513 (2012), arXiv:1206.4141 [hep-lat].
- [15] K. G. Wilson, Confinement of Quarks, *Phys. Rev. D* **10**, 2445 (1974).
- [16] Y. Aoki *et al.* (Flavour Lattice Averaging Group (FLAG)), FLAG Review 2021, *Eur. Phys. J. C* **82**, 869 (2022), arXiv:2111.09849 [hep-lat].
- [17] R. A. Briceno, J. J. Dudek, and R. D. Young, Scattering processes and resonances from lattice QCD, *Rev. Mod. Phys.* **90**, 025001 (2018), arXiv:1706.06223 [hep-lat].
- [18] R. L. Workman *et al.* (Particle Data Group), Review of Particle Physics, *PTEP* **2022**, 083C01 (2022).
- [19] F. Aceti and E. Oset, Wave functions of composite hadron states and relationship to couplings of scattering amplitudes for general partial waves, *Phys. Rev. D* **86**, 014012 (2012), arXiv:1202.4607 [hep-ph].
- [20] R. L. Jaffe, Ordinary and extraordinary hadrons, *AIP Conf. Proc.* **964**, 1 (2007), arXiv:hep-ph/0701038.
- [21] J. R. Pelaez, On the Nature of light scalar mesons from their large N(c) behavior, *Phys. Rev. Lett.* **92**, 102001 (2004), arXiv:hep-ph/0309292.
- [22] J. R. Pelaez and G. Rios, Nature of the  $f_0(600)$  from its N(c) dependence at two loops in unitarized Chiral Perturbation Theory, *Phys. Rev. Lett.* **97**, 242002 (2006), arXiv:hep-ph/0610397.
- [23] C. B. Lang, D. Mohler, S. Prelovsek, and M. Vidmar, Coupled channel analysis of the rho meson decay in lattice QCD, *Phys. Rev. D* **84**, 054503 (2011), [Erratum: *Phys.Rev.D* 89, 059903 (2014)], arXiv:1105.5636 [hep-lat].
- [24] S. Aoki *et al.* (CS),  $\rho$  Meson Decay in 2+1 Flavor Lattice QCD, *Phys. Rev. D* **84**, 094505 (2011), arXiv:1106.5365 [hep-lat].
- [25] G. S. Bali, S. Collins, A. Cox, G. Donald, M. Göckeler, C. B. Lang, and A. Schäfer (RQCD),  $\rho$  and  $K^*$  resonances on the lattice at nearly physical quark masses and  $N_f = 2$ , *Phys. Rev. D* **93**, 054509 (2016), arXiv:1512.08678 [hep-lat].
- [26] D. J. Wilson, R. A. Briceno, J. J. Dudek, R. G. Edwards, and C. E. Thomas, Coupled  $\pi\pi$ ,  $K\bar{K}$  scattering in  $P$ -wave and the  $\rho$  resonance from lattice QCD, *Phys. Rev. D* **92**, 094502 (2015), arXiv:1507.02599 [hep-ph].
- [27] J. J. Dudek, R. G. Edwards, and C. E. Thomas (Hadron Spectrum), Energy dependence of the  $\rho$  resonance in  $\pi\pi$  elastic scattering from lattice QCD, *Phys. Rev. D* **87**, 034505 (2013), [Erratum: *Phys.Rev.D* 90, 099902 (2014)], arXiv:1212.0830 [hep-ph].
- [28] M. Werner *et al.* (Extended Twisted Mass), Hadron-Hadron Interactions from  $N_f = 2 + 1 + 1$  Lattice QCD: The  $\rho$ -resonance, *Eur. Phys. J. A* **56**, 61 (2020), arXiv:1907.01237 [hep-lat].
- [29] C. Alexandrou, L. Leskovec, S. Meinel, J. Negele, S. Paul, M. Petschlies, A. Pochinsky, G. Rendon, and S. Syritsyn,  $P$ -wave  $\pi\pi$  scattering and the  $\rho$  resonance from lattice QCD, *Phys. Rev. D* **96**, 034525 (2017), arXiv:1704.05439 [hep-lat].
- [30] C. Pelissier and A. Alexandru, Resonance parameters of the rho-meson from asymmetrical lattices, *Phys. Rev. D* **87**, 014503 (2013), arXiv:1211.0092 [hep-lat].
- [31] X. Feng, K. Jansen, and D. B. Renner, Resonance Parameters of the rho-Meson from Lattice QCD, *Phys. Rev. D* **83**, 094505 (2011), arXiv:1011.5288 [hep-lat].
- [32] D. Guo, A. Alexandru, R. Molina, and M. Döring, Rho resonance parameters from lattice QCD, *Phys. Rev. D* **94**, 034501 (2016), arXiv:1605.03993 [hep-lat].
- [33] Z. Fu and L. Wang, Studying the  $\rho$  resonance parameters with staggered fermions, *Phys. Rev. D* **94**, 034505 (2016), arXiv:1608.07478 [hep-lat].

- [34] C. Andersen, J. Bulava, B. Hörz, and C. Morningstar, The  $I = 1$  pion-pion scattering amplitude and timelike pion form factor from  $N_f = 2 + 1$  lattice QCD, Nucl. Phys. B **939**, 145 (2019), arXiv:1808.05007 [hep-lat].
- [35] M. Fischer, B. Kostrzewa, M. Mai, M. Petschlies, F. Pittler, M. Ueding, C. Urbach, and M. Werner (Extended Twisted Mass, ETM), The  $\rho$ -resonance from  $N_f = 2$  lattice QCD including the physical pion mass, Phys. Lett. B **819**, 136449 (2021), arXiv:2006.13805 [hep-lat].
- [36] A. Rodas, J. J. Dudek, and R. G. Edwards, The quark mass dependence of  $\pi\pi$  scattering in isospin 0, 1 and 2 from lattice QCD, (2023), arXiv:2303.10701 [hep-lat].
- [37] B. Hu, R. Molina, M. Döring, M. Mai, and A. Alexandru, Chiral extrapolations of the  $\rho(770)$  meson in  $N_f = 2 + 1$  lattice QCD simulations, Phys. Rev. D **96**, 034520 (2017), arXiv:1704.06248 [hep-lat].
- [38] B. Hu, R. Molina, M. Döring, and A. Alexandru, Two-flavor Simulations of the  $\rho(770)$  and the Role of the  $K\bar{K}$  Channel, Phys. Rev. Lett. **117**, 122001 (2016), arXiv:1605.04823 [hep-lat].
- [39] M. Doring, J. Haidenbauer, U.-G. Meissner, and A. Rusetsky, Dynamical coupled-channel approaches on a momentum lattice, Eur. Phys. J. A **47**, 163 (2011), arXiv:1108.0676 [hep-lat].
- [40] M. Doring, U. G. Meissner, E. Oset, and A. Rusetsky, Scalar mesons moving in a finite volume and the role of partial wave mixing, Eur. Phys. J. A **48**, 114 (2012), arXiv:1205.4838 [hep-lat].
- [41] J.-J. Wu, T. S. H. Lee, A. W. Thomas, and R. D. Young, Finite-volume Hamiltonian method for coupled-channels interactions in lattice QCD, Phys. Rev. C **90**, 055206 (2014), arXiv:1402.4868 [hep-lat].
- [42] Z.-W. Liu, W. Kamleh, D. B. Leinweber, F. M. Stokes, A. W. Thomas, and J.-J. Wu, Hamiltonian effective field theory study of the  $N^*(1440)$  resonance in lattice QCD, Phys. Rev. D **95**, 034034 (2017), arXiv:1607.04536 [nucl-th].
- [43] J.-j. Wu, D. B. Leinweber, Z.-w. Liu, and A. W. Thomas, Structure of the Roper Resonance from Lattice QCD Constraints, Phys. Rev. D **97**, 094509 (2018), arXiv:1703.10715 [nucl-th].
- [44] Z.-W. Liu, J. M. M. Hall, D. B. Leinweber, A. W. Thomas, and J.-J. Wu, Structure of the  $\Lambda(1405)$  from Hamiltonian effective field theory, Phys. Rev. D **95**, 014506 (2017), arXiv:1607.05856 [nucl-th].
- [45] Z.-W. Liu, W. Kamleh, D. B. Leinweber, F. M. Stokes, A. W. Thomas, and J.-J. Wu, Hamiltonian effective field theory study of the  $N^*(1535)$  resonance in lattice QCD, Phys. Rev. Lett. **116**, 082004 (2016), arXiv:1512.00140 [hep-lat].
- [46] Z. Yang, G.-J. Wang, J.-J. Wu, M. Oka, and S.-L. Zhu, Novel Coupled Channel Framework Connecting the Quark Model and Lattice QCD for the Near-threshold Ds States, Phys. Rev. Lett. **128**, 112001 (2022), arXiv:2107.04860 [hep-ph].
- [47] Y. Li, J.-J. Wu, C. D. Abell, D. B. Leinweber, and A. W. Thomas, Partial Wave Mixing in Hamiltonian Effective Field Theory, Phys. Rev. D **101**, 114501 (2020), arXiv:1910.04973 [hep-lat].
- [48] Y. Li, J.-j. Wu, D. B. Leinweber, and A. W. Thomas, Hamiltonian effective field theory in elongated or moving finite volume, Phys. Rev. D **103**, 094518 (2021), arXiv:2103.12260 [hep-lat].
- [49] S. Weinberg, *The Quantum theory of fields. Vol. 1: Foundations* (Cambridge University Press, 2005).
- [50] A. Matsuyama, T. Sato, and T. S. H. Lee, Dynamical coupled-channel model of meson production reactions in the nucleon resonance region, Phys. Rept. **439**, 193 (2007), arXiv:nucl-th/0608051.
- [51] D. B. Leinweber, A. W. Thomas, K. Tsushima, and S. V. Wright, Chiral behavior of the rho meson in lattice QCD, Phys. Rev. D **64**, 094502 (2001), arXiv:hep-lat/0104013.
- [52] J.-J. Wu, T. S. H. Lee, and B. S. Zou, Nucleon Resonances with Hidden Charm in Coupled-Channel Models, Phys. Rev. C **85**, 044002 (2012), arXiv:1202.1036 [nucl-th].
- [53] V. Bernard, M. Lage, U.-G. Meissner, and A. Rusetsky, Resonance properties from the finite-volume energy spectrum, JHEP **08**, 024, arXiv:0806.4495 [hep-lat].
- [54] C. R. Allton, W. Armour, D. B. Leinweber, A. W. Thomas, and R. D. Young, Chiral and continuum extrapolation of partially-quenched lattice results, Phys. Lett. B **628**, 125 (2005), arXiv:hep-lat/0504022.
- [55] P. C. Bruns and U.-G. Meissner, Infrared regularization for spin-1 fields, Eur. Phys. J. C **40**, 97 (2005), arXiv:hep-ph/0411223.
- [56] W. Armour, C. R. Allton, D. B. Leinweber, A. W. Thomas, and R. D. Young, Unified chiral analysis of the vector meson spectrum from lattice QCD, J. Phys. G **32**, 971 (2006), arXiv:hep-lat/0510078.
- [57] F. James and M. Roos, Minuit: A System for Function Minimization and Analysis of the Parameter Errors and Correlations, Comput. Phys. Commun. **10**, 343 (1975).
- [58] C. D. Abell, D. B. Leinweber, A. W. Thomas, and J.-J. Wu, Regularization in nonperturbative extensions of effective field theory, Phys. Rev. D **106**, 034506 (2022), arXiv:2110.14113 [hep-lat].
- [59] F. Kleefeld, E. van Beveren, and G. Rupp, The Pionic width of the omega(782) meson within a well-defined, unitary quantum field theory of (anti-)particles and (anti-)holes, Nucl. Phys. A **694**, 470 (2001), arXiv:hep-ph/0101247.
- [60] S. D. Protopopescu, M. Alston-Garnjost, A. Barbaro-Galtieri, S. M. Flatte, J. H. Friedman, T. A. Lasinski, G. R. Lynch, M. S. Rabin, and F. T. Solmitz, Pi pi Partial Wave Analysis from Reactions  $\pi^+ p \rightarrow \pi^+ \pi^- \Delta^{++}$  and  $\pi^+ p \rightarrow K^+ K^- \Delta^{++}$  at 7.1-GeV/c, Phys. Rev. D **7**, 1279 (1973).
- [61] P. Estabrooks and A. D. Martin, pi pi Phase Shift Analysis Below the K anti-K Threshold, Nucl. Phys. B **79**, 301 (1974).
- [62] B. Hyams *et al.*,  $\pi\pi$  Phase Shift Analysis from 600-MeV to 1900-MeV, Nucl. Phys. B **64**, 134 (1973).
- [63] S. Aoki and T. Doi, Lattice QCD and baryon-baryon interactions: HAL QCD method, Front. in Phys. **8**, 307 (2020), arXiv:2003.10730 [hep-lat].

### Appendix A: The formulas for $\mathbf{n} \leftrightarrow \mathbf{k}^*(\mathbf{n})$ and $e_n$

Here, we will list all cases involved in our present calculation, since the transformation  $\mathbf{n} \leftrightarrow \mathbf{k}^*(\mathbf{n})$  and  $e_n$  differ from how the momentum is quantized. A summary is given here.

1. If quantized in a cubic box with total momentum  $\mathbf{P} = 0$  and length  $L$ , then  $\mathbf{k}^*(\mathbf{n}) = \frac{2\pi}{L}\mathbf{n}$ , and  $e_n = n^2$ .
2. If quantized in a elongated box with total momentum  $\mathbf{P} = 0$ , then  $\mathbf{k}^*(\mathbf{n}) = \frac{2\pi}{L}(\mathbf{n}_\perp + \frac{1}{\eta}\mathbf{n}_\parallel)$  where  $\eta > 1$  denotes the elongation strength,  $\perp$  and  $\parallel$  denotes the vertical and parallel component to the elongated direction named  $\mathbf{d}$ , respectively. Then  $e_n$  need two values,  $n^2$  and  $|\mathbf{n} \cdot \mathbf{d}|$ .
3. If quantized in a cubic box with total momentum  $\mathbf{P} \equiv 2\pi\mathbf{d}/L \neq 0$ , then  $\mathbf{k}^*(\mathbf{n}) = \mathbf{k}^*(\mathbf{k}(\mathbf{n}))$  and  $\mathbf{k}(\mathbf{n}) = \frac{2\pi}{L}\mathbf{n}$  where  $\mathbf{k}^*(\mathbf{k})$  is the ‘‘Lorentz-like transformation’’ for channel  $\alpha$  defined as

$$\mathbf{k}^*(\mathbf{k}) = \mathbf{k}_\perp + \gamma \left( \mathbf{k}_\parallel - \frac{E_{\alpha_1}(\mathbf{k})}{E_{\alpha_1}(\mathbf{k}) + E_{\alpha_2}(\mathbf{P} - \mathbf{k})} \mathbf{P} \right),$$

$$\gamma = \frac{E_{\alpha_1}(\mathbf{k}) + E_{\alpha_2}(\mathbf{P} - \mathbf{k})}{\sqrt{(E_{\alpha_1}(\mathbf{k}) + E_{\alpha_2}(\mathbf{P} - \mathbf{k}))^2 - \mathbf{P}^2}}, \quad (\text{A1})$$

where  $\mathbf{k}_\parallel = (\mathbf{k} \cdot \mathbf{P})\mathbf{P}/\mathbf{P}^2$  and  $\mathbf{k}_\perp = \mathbf{k} - \mathbf{k}_\parallel$ . Correspondingly the Jacobian is

$$\mathbf{J}(\mathbf{k}) = \frac{E_{\alpha_1}(\mathbf{k}) + E_{\alpha_2}(\mathbf{P} - \mathbf{k})}{E_{\alpha_1}(\mathbf{k}) E_{\alpha_2}(\mathbf{P} - \mathbf{k})} \bigg/ \frac{E_{\alpha_1}(\mathbf{k}^*) + E_{\alpha_2}(\mathbf{k}^*)}{E_{\alpha_1}(\mathbf{k}^*) E_{\alpha_2}(\mathbf{k}^*)}. \quad (\text{A2})$$

And the  $e_n$  also needs two values,  $n^2$  and  $\mathbf{n} \cdot \mathbf{d}$ . Furthermore, please note that for the  $\pi\pi$  case, the two values are unordered.

4. If quantized in a elongated box with total momentum  $\mathbf{P} \neq 0$  and  $\mathbf{P}$  is parallel to the elongated direction  $\mathbf{d}$ , it is same as the third case above except that  $\mathbf{k}(\mathbf{n}) = \frac{2\pi}{L}(\mathbf{n}_\perp + \frac{1}{\eta}\mathbf{n}_\parallel)$ . And the  $e_n$  are also the same as that in the third case.

### Appendix B: Determination of fixed parameters in Scheme C

In this appendix the determination of  $g_{\omega\rho\pi}$  and  $\Lambda_{\omega\rho\pi}$  are discussed. As mentioned in the main text, besides lattice spectrum the parameters should also be constrained by the decay width  $\Gamma_{\omega \rightarrow 3\pi}$  as well as phase shift  $\delta_{\pi\pi \rightarrow \pi\pi}^{\ell=1}$  on the experimental side.

The decay channel  $\omega \rightarrow 3\pi$  is believed to be dynamically dominated by the  $\omega \rightarrow \rho\pi \rightarrow 3\pi$  mechanism. Therefore, the calculation of the decay width would concern  $V_{\pi\pi}$  and  $V_{\omega\pi}$  defined in Eq.(7) and (8). States in this appendix are normalized as  $\langle \mathbf{p} | \mathbf{k} \rangle = (2\pi)^3 2E_p \delta^3(\mathbf{k} - \mathbf{p})$  unless specified other. Let  $|p_1^+ p_2^- p_3^0\rangle$  and  $T^\lambda(E; p_1, p_2, p_3)$  denote  $|\pi^+(\mathbf{p}_1) \pi^-(\mathbf{p}_2) \pi^0(\mathbf{p}_3)\rangle$  and T-matrix element  $\langle p_1^+ p_2^- p_3^0 | T(E) | \omega, \lambda \rangle$  with  $\lambda$  being the polarization of the  $\omega$ , respectively. Then,

$$T^\lambda(E; p_1, p_2, p_3) = \int \frac{d^3\mathbf{q}}{(2\pi)^6 2E_\rho(\mathbf{q}) 2E_\pi(\mathbf{q})} \sum_\sigma T_\sigma^{I=0}(E; p_1 p_2 p_3; \mathbf{q}) \frac{1}{E - E_\rho(\mathbf{q}) - E_\pi(\mathbf{q})} V_{\omega \rightarrow \rho\pi}^{\lambda\sigma}(\mathbf{q}) \quad (\text{B1})$$

where  $\sigma$  denotes the polarization of  $\rho$  and

$$T_\sigma^{I=0}(E; p_1 p_2 p_3; \mathbf{q}) \equiv \langle p_1^+ p_2^- p_3^0 | T^{I=0}(E) | \rho(-\mathbf{q}) \pi(\mathbf{q}); \sigma \rangle \quad (\text{B2})$$

$$V_{\omega \rightarrow \rho\pi}^{\lambda\sigma}(\mathbf{q}) \equiv \langle \rho(-\mathbf{q}) \pi(\mathbf{q}); \sigma | V^{I=0} | \omega, \lambda \rangle \quad (\text{B3})$$

With straightforward calculation it can be shown that

$$T^\lambda(E; p_1, p_2, p_3) = A_{12}^\lambda(E) + A_{23}^\lambda(E) + A_{31}^\lambda(E)$$

where  $A_{ij}^\lambda(E)$  is short for  $A^\lambda(E; p_i, p_j)$  given by

$$A^\lambda(E; p, k) = \sqrt{\frac{1}{6}} \sum_\sigma \frac{1}{(2\pi)^3 2E_\rho(\mathbf{k})} V_{\rho \rightarrow \pi\pi}^\sigma(\mathbf{p}^*) \frac{W(E; \mathbf{k}) - m_\rho^B}{W(E; \mathbf{k}) - m_\rho^B - \Sigma(W(E; \mathbf{k}))} \frac{1}{E - E_\rho(\mathbf{k}) - E_\pi(\mathbf{k})} V_{\omega \rightarrow \rho\pi}^{\lambda\sigma}(\mathbf{k}) \quad (\text{B4})$$

where  $\sqrt{\frac{1}{6}}$  is the isospin factor,  $\Sigma = \Sigma_{\pi\pi} + \Sigma_{\omega\pi}$  defined in

Eq.(16,17),  $\mathbf{p}^*$  is the momentum  $\mathbf{p}$  boosted in  $\rho$  rest frame



since we have boosted the T-matrix element into  $\rho$  rest frame and  $W(E; \mathbf{k}) \equiv \sqrt{(E - E_\pi(\mathbf{k}))^2 - \mathbf{k}^2}$ . Therefore, the spin-averaged decay width is given by

$$\begin{aligned} \bar{\Gamma} &= \frac{(2\pi)^4}{(2\pi)^6 2m_\omega} \frac{1}{3} \sum_\lambda \int d\Phi_3 |T^\lambda(m_\omega; p_1, p_2, p_3)|^2 \quad (\text{B5}) \\ &= \frac{(2\pi)^4}{(2\pi)^6 2m_\omega} \int d\Phi_3 \sum_\lambda \left\{ |A_{23}^\lambda(m_\omega)|^2 + \right. \\ &\quad \left. 2 \operatorname{Re} (A_{23}^\lambda(m_\omega) A_{31}^{\lambda*}(m_\omega)) \right\} \quad (\text{B6}) \end{aligned}$$

where  $d\Phi_3$  is the Lorentz-invariant three-body phase space element defined in [18]. It is convenient to take  $d\Phi_3 \propto dm_{12} d\Omega_3 d\Omega_1^*$  and  $\propto dm_{12}^2 dm_{23}^2 d\Omega_{\text{Euler}}$  for the integration of  $|A|$  term and interference term, respectively.  $V_{\rho \rightarrow \pi\pi}^\sigma$  and  $V_{\omega \rightarrow \rho\pi}^{\lambda\sigma}$  can be written as two forms. The manifestly Lorentz-invariant one is convenient for the integration of THE interference term and the other

for THE  $|A|^2$  term,

$$V_{\rho \rightarrow \pi\pi}^\sigma(\mathbf{k}) = -(2\pi)^3 \sqrt{2} g_{\rho\pi\pi} \epsilon_\mu(\mathbf{0}, \sigma) (k_1^* - k_2^*)^\mu u_{\pi\pi} \quad (\text{B7})$$

$$= (2\pi)^{\frac{9}{2}} \left( \sqrt{2E_\pi(\mathbf{k})} \right)^2 \sqrt{2m_\rho^B} Y_{1\sigma}(\hat{\mathbf{k}}) V_{\pi\pi}(\mathbf{k}) \quad (\text{B8})$$

$$\begin{aligned} V_{\omega \rightarrow \rho\pi}^{\lambda\sigma}(\mathbf{k}) &= (2\pi)^3 \sqrt{3} g_{\omega\rho\pi} \epsilon^{\mu\nu\alpha\beta} P_\mu \epsilon_\nu(\mathbf{0}, \lambda) P'_\alpha \epsilon'_\beta(-\mathbf{k}, \sigma) \quad (\text{B9}) \\ &= -\sqrt{8\pi} (2\pi)^3 m_\omega g_{\omega\rho\pi} C_{11}(1\lambda; \lambda - \sigma\sigma) Y_{\lambda-\sigma}^1(\hat{\mathbf{k}}) |\mathbf{k}| \quad (\text{B10}) \end{aligned}$$

where  $\epsilon$  is the polarization vector,  $u_{\pi\pi}$  and  $V_{\pi\pi}$  are the form factor and potential defined in Eq.(9) and Eq.(7), respectively.  $p_{1/2}^*$  are the four-vectors of  $\pi$ ,  $P$  and  $P'$  are the four-vectors of  $\omega$  and  $\rho$ , respectively. We do not introduce a form factor for  $V_{\omega \rightarrow \rho\pi}$  since there is no loop integral related to it. Following that in Ref.[59], the interference term is given by,

$$\begin{aligned} \sum_\lambda \operatorname{Re} (A_{23}^\lambda(m_\omega) A_{31}^{\lambda*}(m_\omega)) &= \frac{(2\pi)^6 g_{\rho\pi\pi}^2 g_{\omega\rho\pi}^2}{4E_\rho(\mathbf{p}_3) E_\rho(\mathbf{p}_1)} \frac{(m_{12} - m_\rho^B)(m_{23} - m_\rho^B)}{(m_\omega - E_\rho(\mathbf{p}_3) - E_\pi(\mathbf{p}_3))(m_\omega - E_\rho(\mathbf{p}_1) - E_\pi(\mathbf{p}_1))} u_{\pi\pi}(\mathbf{p}_1^*) u_{\pi\pi}(\mathbf{p}_1) \\ &\times \operatorname{Re} \left[ \frac{1}{m_{12} - m_\rho^B - \Sigma(m_{12})} \left( \frac{1}{m_{23} - m_\rho^B - \Sigma(m_{23})} \right)^* \right] \begin{vmatrix} P^2 & P \cdot (p_2 + p_3) & P \cdot (p_3 - p_2) \\ P \cdot (p_1 + p_2) & (p_1 + p_2) \cdot (p_2 + p_3) & (p_1 + p_2) \cdot (p_3 - p_2) \\ P \cdot (p_2 - p_1) & (p_2 - p_1) \cdot (p_2 + p_3) & (p_2 - p_1) \cdot (p_3 - p_2) \end{vmatrix} \quad (\text{B11}) \end{aligned}$$

$|\mathbf{p}_1|, |\mathbf{p}_3|$  and the elements in the determinant can be easily expressed in terms of  $m_{12}^2$  and  $m_{23}^2$ . On the other

hand, the  $|A^\lambda|^2$  term is given by

$$\begin{aligned} \int d\Omega_3 d\Omega_1^* \sum_\lambda |A_{23}^\lambda(m_\omega)|^2 &= \frac{m_\omega^2}{2} \left( \frac{1}{(2\pi)^3 2E_\rho(\mathbf{p}_3)} \right)^2 \left( \frac{1}{m_\omega - E_\rho(\mathbf{p}_3) - E_\pi(\mathbf{p}_3)} \right)^2 \left| \frac{W(m_\omega; \mathbf{p}_3) - m_\rho^B}{W(m_\omega; \mathbf{p}_3) - m_\rho^B - \Sigma(W(m_\omega; \mathbf{p}_3))} \right|^2 \\ &\times \left( (2\pi)^3 2\sqrt{2} g_{\rho\pi\pi} |\mathbf{p}_1^*| u_{\pi\pi}(|\mathbf{p}_1^*|) \right)^2 \left( (2\pi)^3 \sqrt{8\pi} m_\omega g_{\omega\rho\pi} |\mathbf{p}_3| \right)^2 \quad (\text{B12}) \end{aligned}$$

With these ingredients  $\Gamma_{\omega \rightarrow \rho\pi \rightarrow 3\pi}$  can then be calculated.

In Sec.(III C) we found that when  $V_{\omega\pi} = 0$ ,  $g_{\rho\pi\pi}$  and  $\Lambda_{\rho\pi\pi}$  can be fixed at 7.07 and 890 MeV, respectively. It is expected that the introduction of the  $\omega\rho\pi$  vertex would slightly shift these parameters, we try to take  $g_{\rho\pi\pi}$  and  $\Lambda_{\rho\pi\pi}$  at 7.40 and 900 MeV, respectively. Besides, we assume that  $\Lambda_{\omega\rho\pi} = \Lambda_{\rho\pi\pi}$ . The remaining two parameters  $m_\rho^B$  and  $g_{\omega\rho\pi}$  are constrained by  $\Gamma_{\omega \rightarrow 3\pi}$  and  $\delta_{\pi\pi \rightarrow \pi\pi}^{\ell=1}$ .

If we adopt  $g_{\omega\rho\pi} = 18/\text{GeV}$ , which is close to that in Ref.[51], and  $m_\rho^B = 870$  MeV, it is found that

$$\Gamma_{\omega \rightarrow \rho\pi \rightarrow 3\pi} = 7.12 \text{ MeV} \quad (\text{B13})$$

while the experimental value of the partial decay width  $\Gamma_{\omega \rightarrow 3\pi}^{\text{ex}} = 7.74(13) \text{ MeV}$ . The 10% discrepancy is accounted for by the neglected direct interaction between the  $|\omega\rangle$  and the  $|3\pi\rangle$  channel[59]. Furthermore, the

phase shift defined by Eq.(19) can also be obtained and shown in Fig.8 The approximate consistence between the theoretical and experimental results justify the values adopted. Furthermore, it is interesting that the extrapolated  $m_\rho^B$  of HSC, MILC and Bulava *et al.* in scheme C are nearly the same as that adopted here.

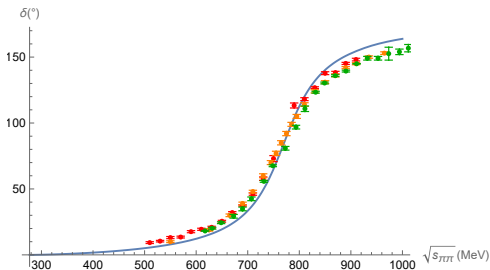


FIG. 8. Phase shift calculation by Eq.(19) using parameters  $g_{\omega\rho\pi} = 18/\text{GeV}$ ,  $\Lambda_{\omega\rho\pi} = \Lambda_{\rho\pi\pi} = 900 \text{ MeV}$ ,  $g_{\rho\pi\pi} = 7.40$  and  $m_\rho^B = 870 \text{ MeV}$  at the physical pion mass  $\mu_\pi$ . The points in the figure are experimental values from Refs. [60–62].

### Appendix C: Table of $C_{\Gamma,G}$

In this appendix the values of  $C_{\Gamma,G}$  are given. As in the main context,  $C_{\Gamma,G}$  is the reduction coefficient. To be more specific, the non-zero space spanned by  $|\alpha; e_n, M\rangle$  furnish a representation labelled by  $\Gamma_\infty$  which is irreducible for  $G_\infty$  but generally reducible for subgroup  $G$ ,

i.e., a restricted representation for  $G$ . Therefore, with  $C_{\Gamma,G}$ , the  $\Gamma_\infty$  can be decompose into the direct sum of the irreducible representation of  $G$ . Furthermore, thanks to the Wigner-Eckart theorem, it is sufficient to take  $a = 1$  without loss of generality. The non-vanishing  $[C_{\Gamma,G}]_{M,a=1}$  relevant to the present work is given in the Table.(VI). For more general result one can refer to, for example, Ref. [47, 48].

$(\Gamma, G)$	$\sum_M [C_{\Gamma,G}]_{M,a=1}  M\rangle$
$(T_1, O_h)$	$\frac{1}{\sqrt{2}}  1\rangle - \frac{1}{\sqrt{2}}  -1\rangle$
$(A_1, C_{4v})$	$ 0\rangle$
$(E, C_{4v})$	$ -1\rangle$
$(A_1, C_{3v})$	$ 0\rangle$
$(E, C_{3v})$	$ -1\rangle$
$(A_1, C_{2v})$	$ 0\rangle$
$(B_1, C_{2v})$	$\frac{1}{\sqrt{2}}  -1\rangle + \frac{1}{\sqrt{2}}  1\rangle$
$(B_2, C_{2v})$	$\frac{1}{\sqrt{2}}  -1\rangle - \frac{1}{\sqrt{2}}  1\rangle$

TABLE VI. Values of  $[C_{\Gamma,G}]_{M,a=1}$  relevant to the present work.  $|M\rangle$  is short for the state  $|\alpha; e_n, M\rangle$  defined in Eq.(24) with  $J = 1$ .

### Appendix D: HEFT fits to lattice QCD spectra

Here, we show all the other fit results for the various lattice QCD data sets collected besides that given in Fig. 1.

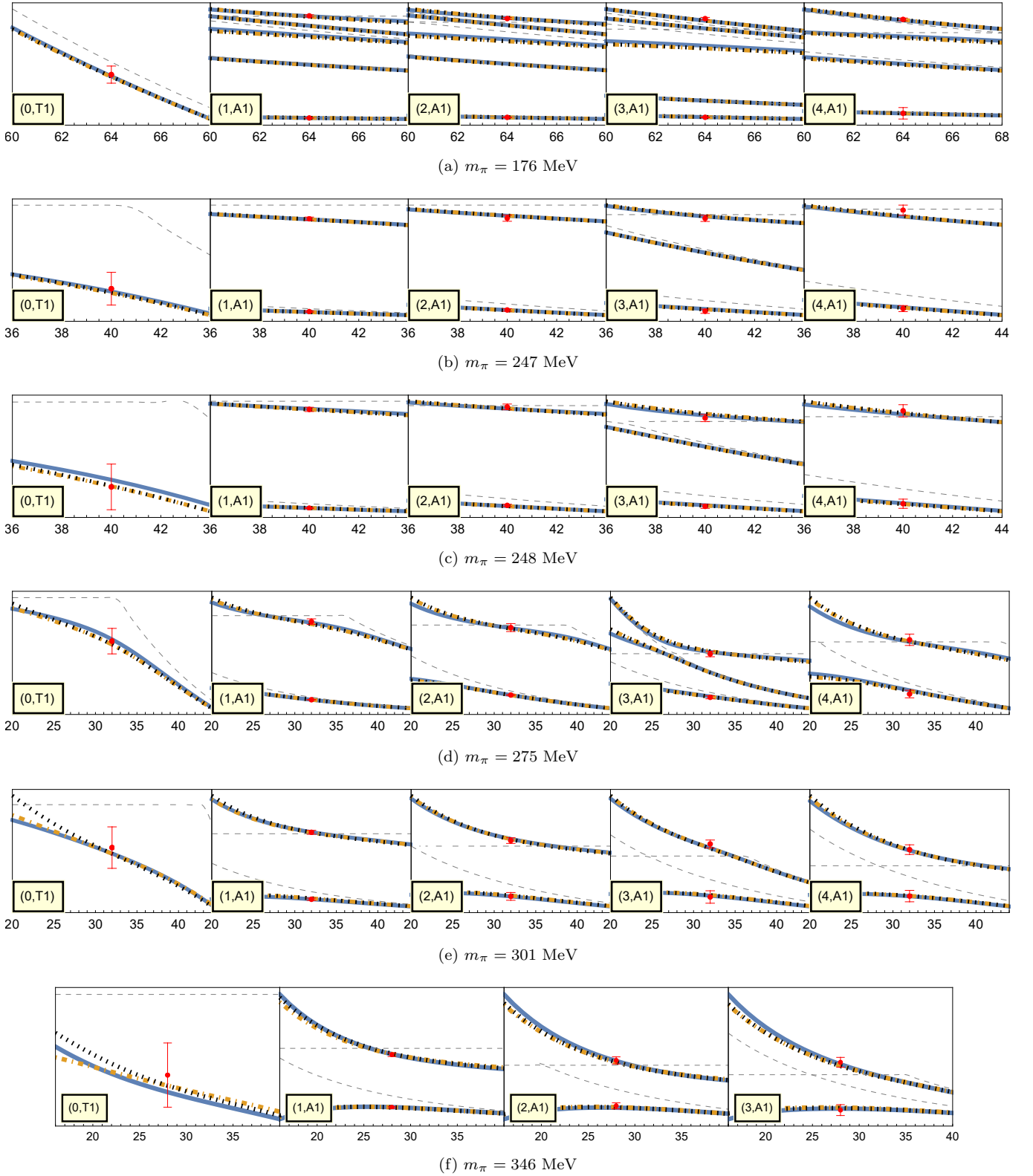


FIG. 9. Same as in Fig. 1 but for the MILC collaboration [33].

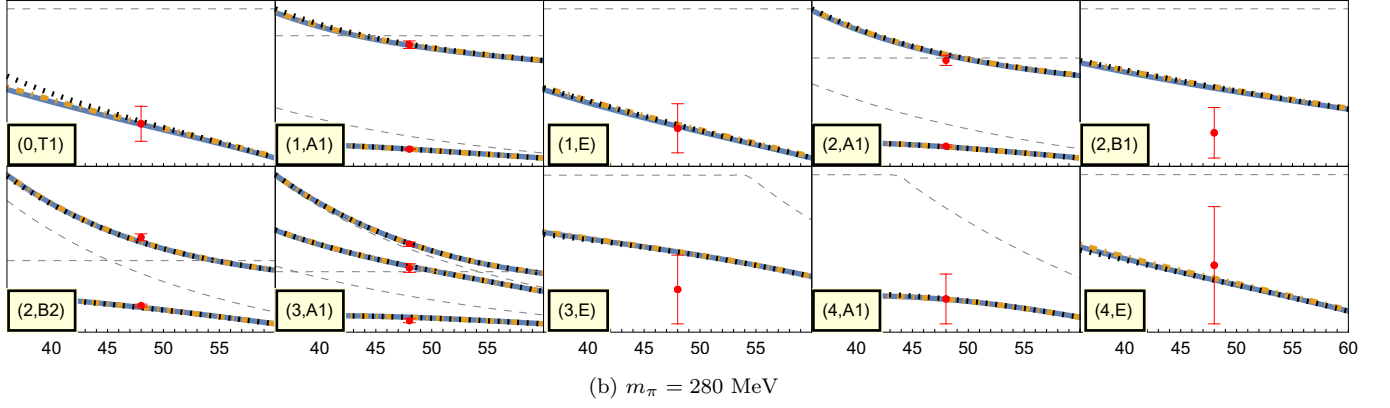
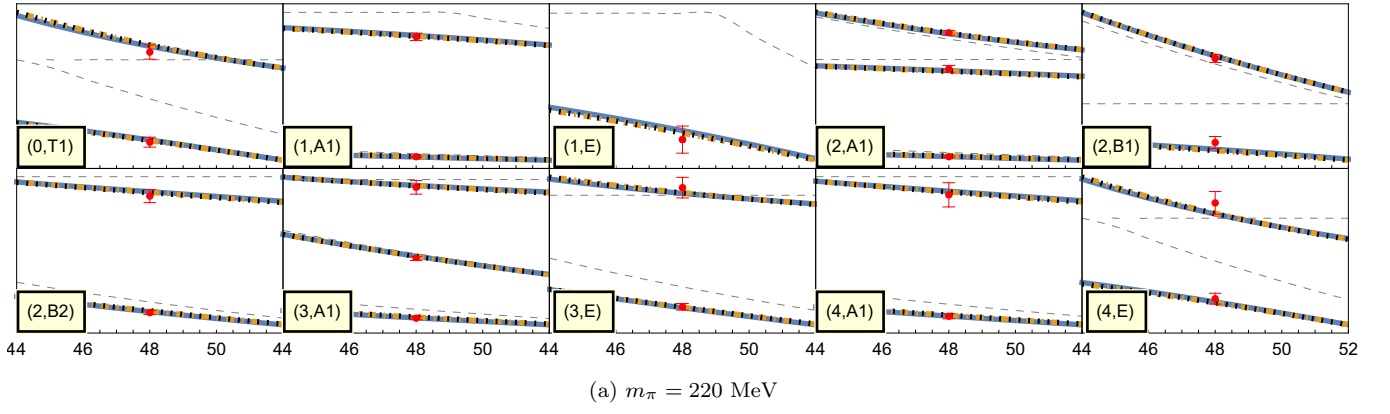


FIG. 10. Same as in Fig. 1 but for other  $m_\pi$  by Bulava *et al.* [34].

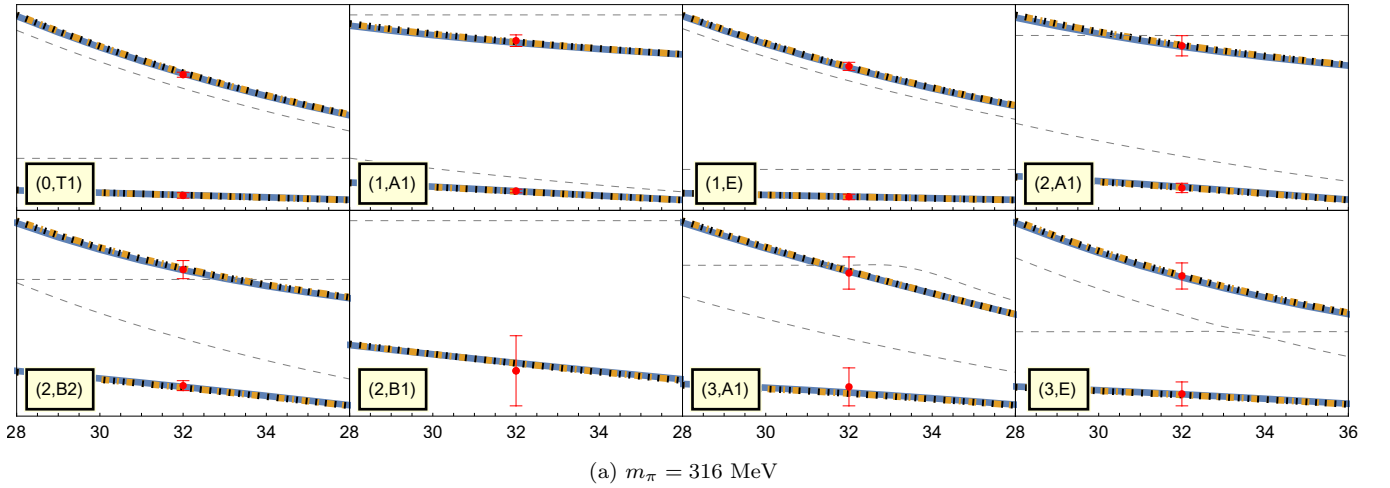


FIG. 11. Same as in Fig. 1 but for C. Alexandru *et al.* [29]

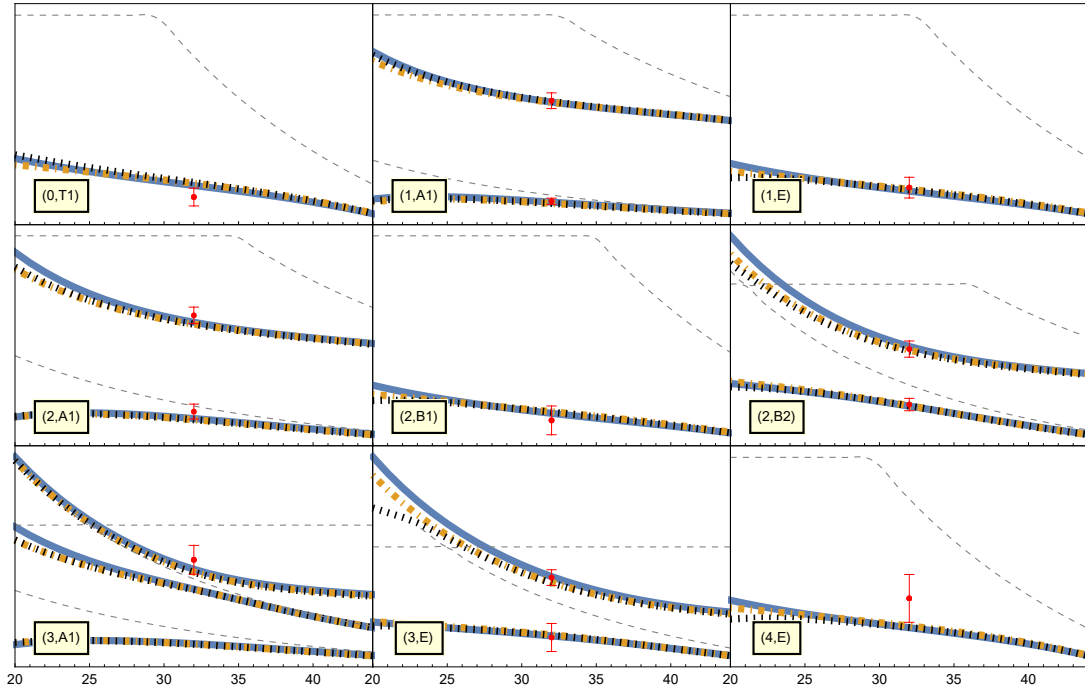
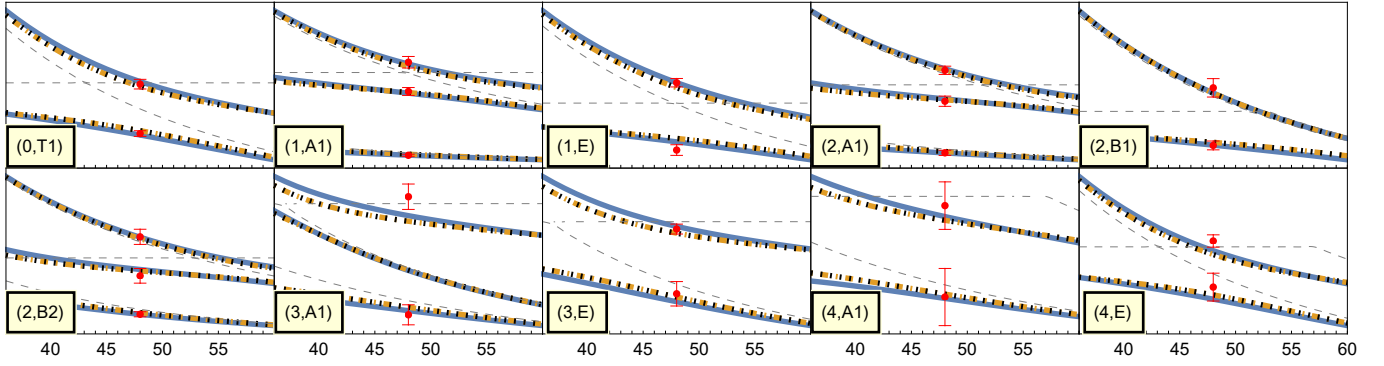
(a)  $m_\pi = 262$  MeV(b)  $m_\pi = 302$  MeV

FIG. 12. Same as in Fig. 1 but for the ETMC collaboration [28].

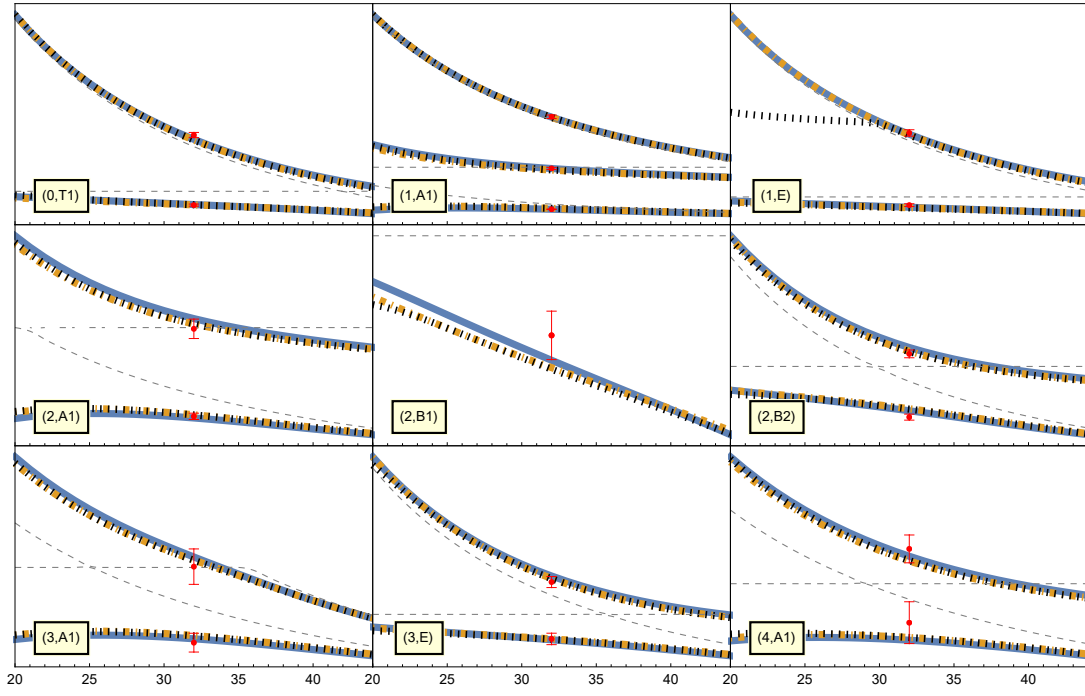
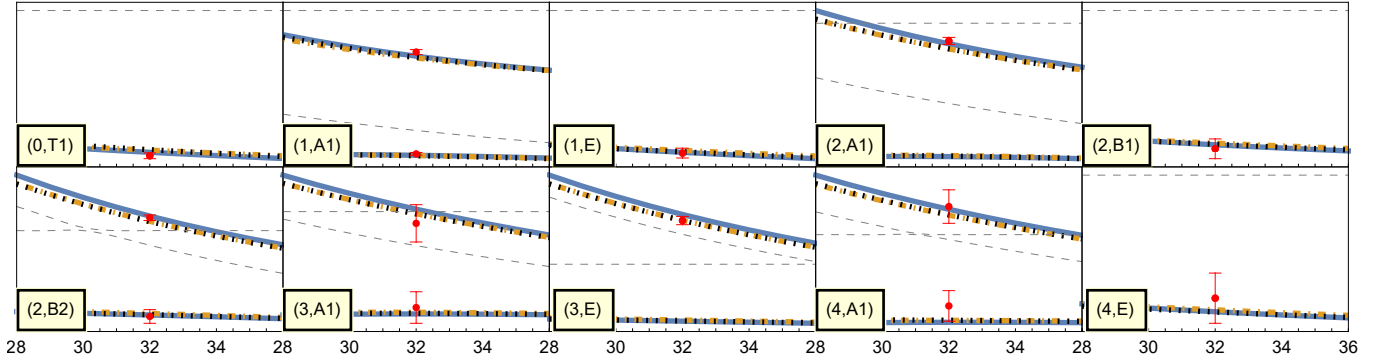
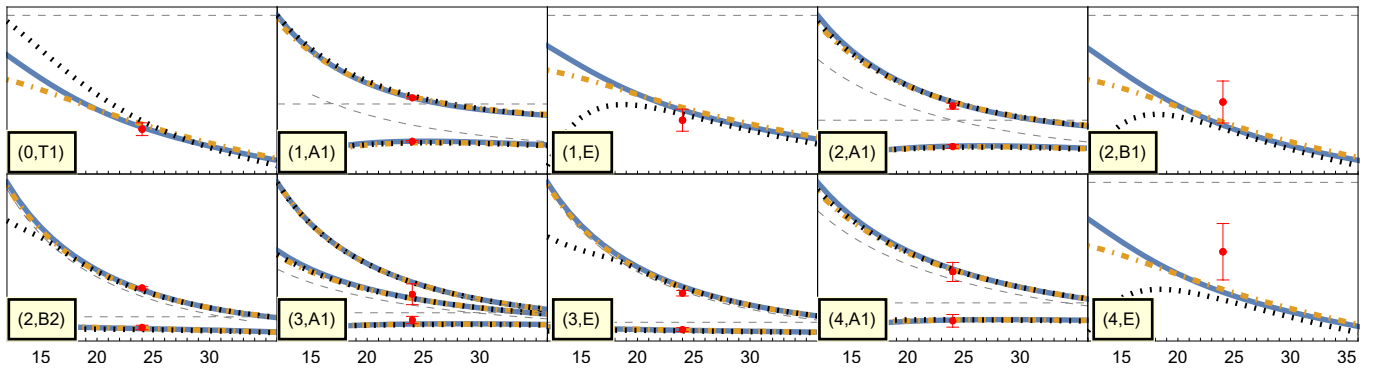
(a)  $m_\pi = 322$  MeV(b)  $m_\pi = 376$  MeV(c)  $m_\pi = 386$  MeV

FIG. 13. Same as in Fig. 1 but for the ETMC collaboration [28]. The turning point of the black dotted line for  $m_\pi = 322$  MeV is due to an avoided level crossing when the  $\omega\pi$  channel is included.

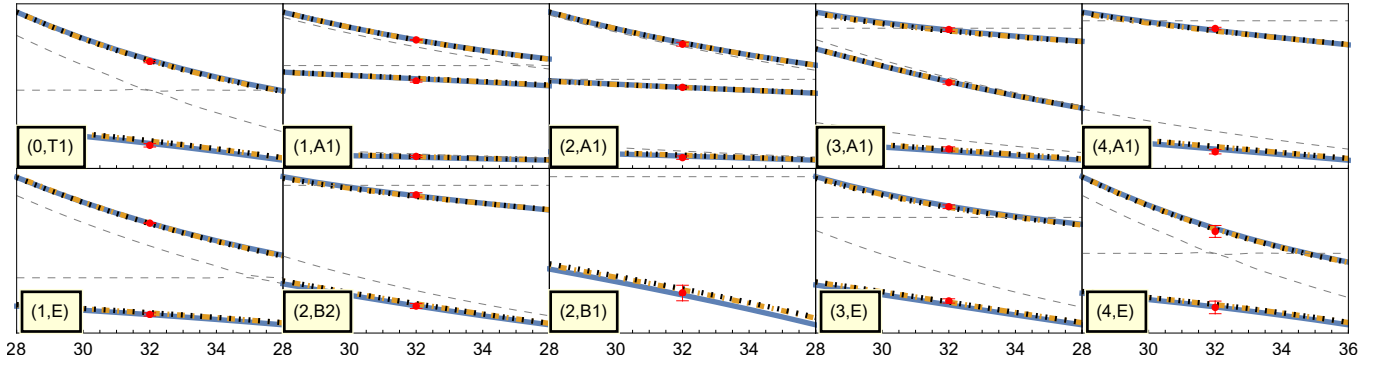
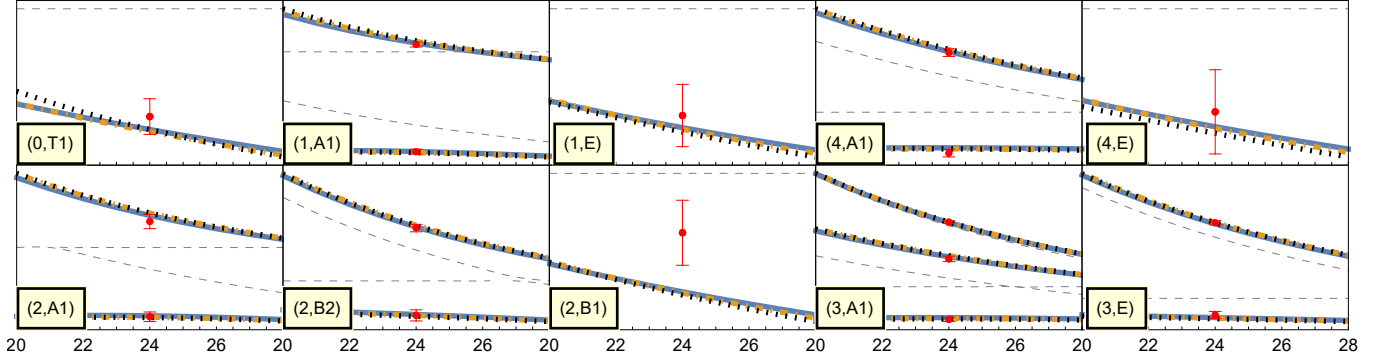
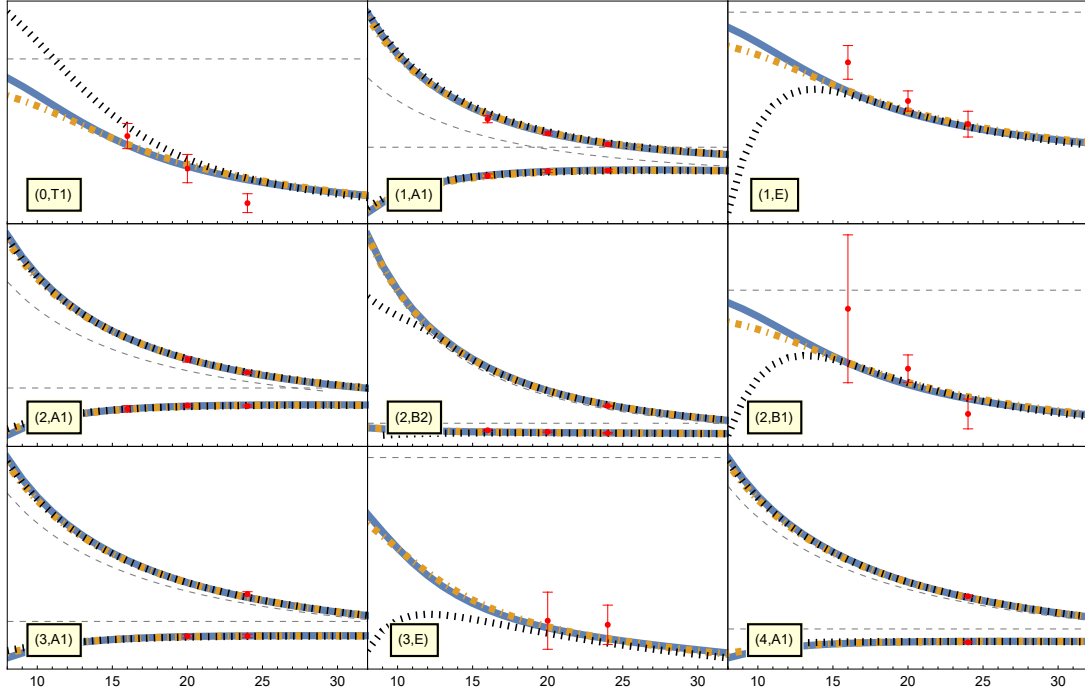
(a)  $m_\pi = 236$  MeV(b)  $m_\pi = 330$  MeV(c)  $m_\pi = 391$  MeV

FIG. 14. Same as in Fig. 1 but for the HSC collaboration [26, 27, 36].

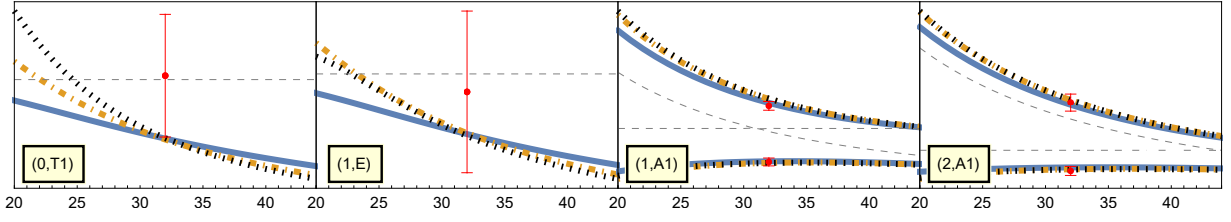


FIG. 15. Same as in Fig. 1 but for the PACS-CS collaboration [63].

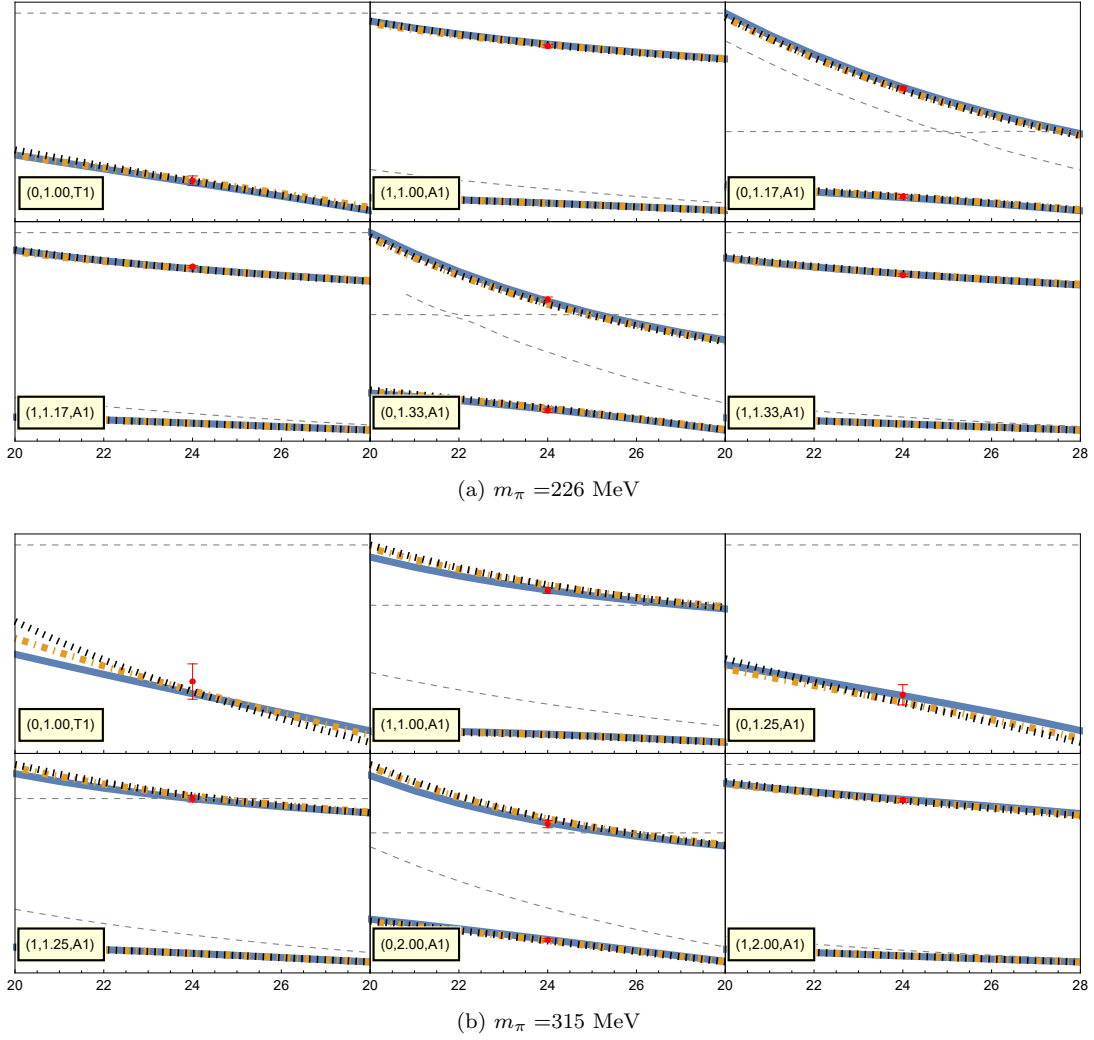


FIG. 16. Same as in Fig. 1 but for Guo *et al.* [32]. Note that there is an additional quantity  $\eta$  denoting the elongation factor in the yellow box compared to the others.